VISCOUS-INVISCID INTERACTIONS OF DENSE GASES

by

Sang-Hyuk Park

Dissertation submitted to the Faculty of the
Virginia Polytechnic Institute and State University
in partial fulfillment of the requirements
for the degree of

DOCTOR OF PHILOSOPHY

in
Engineering Mechanics

APPROVED :

Mark S. Cramer, Chairman

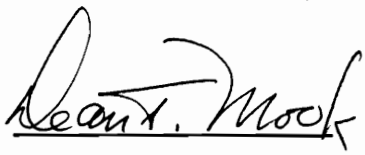

Dean T. Mook

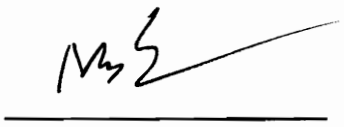

Mahendra P. Singh

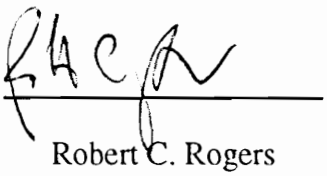

Robert C. Rogers

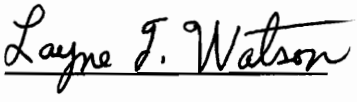

Layne T. Watson

November, 1994

Blacksburg, Virginia

VISCOUS-INVISCID INTERACTIONS OF DENSE GASES

by

Sang-Hyuk Park

Mark S. Cramer, Chairman
Engineering Mechanics

(ABSTRACT)

The interaction of oblique shocks and oblique compression waves with a laminar boundary layer on an adiabatic flat plate is analyzed by solving the Navier-Stokes equations in conservation-law form numerically. The numerical scheme is based on the Beam and Warming's implicit method with approximate factorization. We examine the flow of Bethe-Zel'dovich-Thompson (BZT) fluids at pressures and temperatures on the order of those of the thermodynamic critical point. A BZT fluid is a single-phase gas having specific heat so large that the fundamental derivative of gas dynamics, Γ, is negative over a finite range of pressures and temperatures. The equation of state is the well-known Martin-Hou equation. The main result is the demonstration that the natural dynamics of BZT fluids can suppress boundary layer separation. Physically, this suppression can be attributed to the decrease in adverse pressure gradients associated with the disintegration of compression discontinuities in BZT fluids.

ACKNOWLEDGEMENTS

I would like to thank my advisor, Dr. Cramer, for all his help and support throughout my graduate career. I could not have made it through without his help. I also thank Dr. Layne Watson for his help solving some troubling numerical problems and for providing me with the privilege of using Computer Science Department's alpha machines and other facilities. My thanks go to the other members of my committee, Dr. Dean T. Mook, Dr. Robert C. Rogers, Dr. Mahendra P. Singh, and Dr. Robert A. Heller for their help in the preparation of my dissertation. Finally, many thanks to Dr. Saad A. Ragab, Dr. Bernard Grossman, and Dr. Robert W. Walters for their help in CFD.

Special thanks to the National Science Foundation for supporting research in this area. This work was supported by the National Science Foundation grant number CTS-8913198.

DEDICATED TO :

my Lord Jesus Christ,

my wife Young Hee Oh,

my parents Mr. & Mrs. Eui Won Park and Nam Shik Min, and my parents-in-law Mr. & Mrs. Jin Woo Oh and Soon Bok Sohn,

my two daughters Myung Joon and Hye Joon Park, and my bothers and sister Sang Hee, Sang Sook, and Sang Hwa Park,

my brothers-in-law Yong Mook, Inn Mook, and Kwang Mook Oh,

my friends Kil Jong Yu, Chong Kil Lee, and Moon Hee Lee.

Table of Contents

List of Tables

List of Figures

Chapter 1

Introduction

An important loss mechanism in many transonic and supersonic flows is due to shock-induced boundary layer separation. In addition to significant losses, such separations can set up self-sustained oscillations and therefore may give rise to vibration and noise. In the present investigation we examine one of the most elementary shock-boundary layer interactions, namely, that caused by the reflection of an oblique shock from a rigid surface. A sketch of the complex interaction of a shock wave with a boundary layer is shown in Figure 1.1. Such interactions are prevalent in aerodynamic applications and can also occur in supersonic turbomachinery flows. Our main task is to extend Beam and Warming's implicit factored scheme to account for high pressure, i.e., dense gas, corrections to the gas models. A variety of gases are also studied to check the consistency. We believe that this is the first example of Navier-Stokes calculation for the problem of the interaction of a shock wave with a boundary layer in dense gases. Here we consider a class of fluids of general interest as working fluids for so-called

organic Rankine cycles and demonstrate that the natural dynamics of such gases can reduce and even eliminate shock-induced separation.

The physical mechanism leading to shock-induced separation is due to the strong adverse pressure gradient carried by the incident compression shock. The adverse pressure gradient decelerates the low momentum flow in the boundary layer and if the gradient is strong enough, a backflow, i.e., separation, region can occur. An inspection of even the incompressible Navier-Stokes equations or of the classical Faulkner-Skan flows reveals that it is the magnitude of the spatial gradients, rather than the overall pressure change, which gives rise to separation. Explicit formulas relating the pressure gradient to the onset of separation can be found in the well-known references by Schlichting (1979) and White (1974).

An example which is easily reproduced, is closely related to the main work of the present study, and which illustrates the influence of the pressure gradient on the boundary layer has been computed. A schematic of the flow is depicted in Figure 1.2. The numerical scheme and general configuration are identical to those used later in the present study; full details are given in Chapters 2-4. In this example, the physical problem is that where a sequence of compression waves of increasing width are reflected from a laminar flat plate boundary layer. In each case the fluid is air at a freestream Mach number, pressure, and temperature of 2.0, 0.134 atm, and 308.6 kelvins. Because the pressures are well below those of the thermodynamic critical point, the flow behavior is that of a perfect gas. The strength of each incident compression wave was fixed so that the flow deflection angle was 2.5^0 for each case. The local Reynolds number at the wave impingement point was 2.96×10^5 for each case. The first wave considered was a shock initiated at a distance y_S above the plate. The other two waves were initiated at the same distance upstream of the plate but were of width h centered on

the initiation point of the shock. The resultant skin friction coefficient c_f has been plotted in Figure 1.3. It is seen that the shock is strong enough to separate the laminar boundary layer as evidenced by the region of negative skin friction ($c_f < 0$) on the plate. When the initial width of the compression wave is 36% of the value of y_S, the degree of separation appears to be reduced. In the final case, the total initial width of the compression wave was 72% of y_S. Inspection of the skin friction variation plotted in Figure 1.3 reveals that the adverse pressure gradient in this case is so weak that the boundary layer remains attached. Because the overall pressure rise resulting from the reflection has the same value for each case, this series of examples gives further evidence for the idea that the likelihood of separation depends directly on the width of the incident waves, i.e., on the strength of the adverse pressure gradient, rather than the value of the total pressure rise.

Most of our intuition regarding compressible flows and therefore shock boundary-layer interaction is based on the perfect gas theory. This gas model is an excellent approximation when the pressures and densities are sufficiently low. However, in high-pressure applications, the perfect gas model may not yield accurate predictions of the actual gas response. More complex equations such as the van der Waals, Redlich-Kwong, and Beattie-Bridgeman equations must then be employed. Discussions of these well-known models can be found in most texts on engineering thermodynamics, e.g., Jones and Hawkins (1986). When such high-pressure corrections to the ideal gas equation of state are required we will refer to the fluid as a dense, in contrast to a dilute or low-pressure, gas.

Applications where high-pressure, i.e., dense-gas, effects must be considered include the design of subcritical and supercritical power cycles (Reynolds and Perkins, 1977 and Jones and Hawkins, 1986) and chemical and fuel transport (Leung and

Epstein, 1988 and Bober and Chow, 1990). Further examples include the design of hypersonic and transonic wind tunnels as described by Enkenhus and Parazzoli (1970), Wagner and Schmidt (1978), Simeonides (1987, 1990), Anderson (1991 a,b), and Anders (1993). Dziedzic, et al. (1993) has described the use of supercritical hydrogen to cool hypersonic aircraft. A summary of the nonclassical heat transfer in near-critical CO_2 has been given by Hall (1971) and Hsu and Graham (1976).

Recent studies have revealed that the dynamics of dense gases can differ significantly from those of low pressure gases, particularly when fluids other than air and water are employed. Bethe (1942) and Zel'dovich (1946) were the first to point out that the qualitative behavior of compressible flows depends on the sign of the thermodynamic parameter

$$\Gamma \equiv \frac{a}{\rho} + \frac{\partial a}{\partial \rho}\bigg|_s , \tag{1.1}$$

where ρ and s are the fluid density and entropy and

$$a \equiv \sqrt{\frac{\partial P}{\partial \rho}\bigg|_s} , \tag{1.2}$$

is the thermodynamic sound speed and P is the thermodynamic pressure. The parameter (1.1) is frequently referred to as the fundamental derivative of gas dynamics. Alternate, but equivalent definitions of (1.1) can be found in the articles by Thompson (1971), Lambrakis and Thompson (1972), and Thompson and Lambrakis (1973). The more recent studies of Cramer (1991a, b), Cramer and Best (1991), and Cramer and Crickenberger (1992) reveal that qualitative, but less dramatic, differences may also be observed when $0 < \frac{\rho\Gamma}{a} < 1$.

The value of (1.1) for perfect gases, i.e., gases satisfying the ideal gas law and the condition of constant specific heats, is given by

$$\Gamma = \frac{a}{\rho}\frac{\gamma+1}{2},$$

where γ is the ratio of specific heats. Because $\gamma>1$ for all real gases, $\frac{\rho\Gamma}{a}>1$ whenever the perfect gas approximation is valid. It turns out that *any* fluid having $\frac{\rho\Gamma}{a}>1$ exhibits the same qualitative behavior as a perfect gas.

The full range of values which can be attained by the fundamental derivative are illustrated in Figure 1.4 where (1.1) has been evaluated at a temperature corresponding to that at the thermodynamic critical point of the fluid in question for typical examples of commercially available heat transfer and Rankine cycle fluids. The gas model is that developed by Martin and Hou (1955) ; full details of its implementation can be found in Chapter 3. The main point of interest in these plots is that the scaled value of the fundamental derivative of most fluids has a local minimum at one-half to two-thirds of the critical density. The thermodynamic critical point on the temperature-volume diagram is the point where the saturated-liquid line and the saturated-vapor line meet. The temperature, pressure, and density at the critical point are called the critical temperature, critical pressure, and critical density. In Figure 1.4 and in the remainder of this paper, the subscript c will denote properties evaluated at the thermodynamic critical point. This local minimum usually corresponds to values of $\frac{\rho\Gamma}{a}$ between zero and one. However, some of the heavier heat transfer fluids have a local minimum which correspond to $\Gamma<0$. This trend is seen to be in complete agreement with the work of Lambrakis and Thompson (1972), Thompson and Lambrakis (1973), and Cramer (1989). The dynamics of such negative Γ fluids are the principal focus of the present

study. Because of the contributions of the earliest investigators, we will refer to any substance having $\Gamma<0$ for a finite range of pressures and temperatures in the single-phase regime as Bethe-Zel'dvich-Thompson (BTZ) fluids. For a more complete discussion of the class of fluids of the BZT type we refer the reader to the above-mentioned articles by Bethe, Zel'dovich, and Thompson as well as the more recent reviews of Cramer (1991a) and Menikoff and Plohr (1989).

One of the most striking phenomena associated with BZT fluids is due to the fact that compression shocks violate the entropy inequality whenever $\Gamma<0$ everywhere in the flow of interest. As a result, any compression discontinuity inserted in such a flow will disintegrate to form a centered compression fan analogous to the well-known Prandtl-Meyer expansion fans of the perfect gas theory. The inadmissibility of compression shocks in negative Γ fluids was first pointed out by Bethe (1942) and Zel'dovich (1946). Centered compression fans in the context of steady and unsteady flows of BZT fluids were first described by Thompson (1971) and Wendroff (1972). Although compression shocks disintegrate in flows having $\Gamma<0$ everywhere, expansion shocks, i.e., shocks for which the pressure of a material particle decreases , not only form naturally as result of nonlinear steepening but also satisfy all the relevant admissibility conditions. A complete discussion of the fundamental existence conditions can be found in the recent reviews of Menikoff and Plohr (1989) and Cramer (1991a).

The motivation for the study of the shock-induced separation in BZT fluids becomes clear when we recall that it is both the strength and the width of the incoming wave which determines separation. Even if a compression discontinuity is introduced into a supersonic flow of a $\Gamma<0$ fluid, the natural dynamics will be such that the original discontinuity will arrive at other boundaries, e.g., other turbine blades, in the form of a wave of nonzero width. The resultant pressure gradient experienced by the boundary

layer will be significantly decreased and it may turn out that the boundary layer can remain attached. The goal of the present investigation is to examine whether such a suppression of shock-induced separation can in fact be attained.

A first step toward understanding the dense gas viscous-inviscid interaction was accomplished by Kluwick (1994) who extended the classical triple-deck analysis to include not only gases at high pressure but also those of the BZT type. In the case of purely supersonic flows, the gas dynamic nonlinearity was found to be negligible for the purposes of analyzing the interaction region; this of course is consistent with the conclusions of the classical theory. Thus, for a given incoming (inviscid) signal, we expect no new physics in the interaction zone. We feel this result suggests that any suppression of separation will be due to the differences in the width of the incoming compression wave. The Navier-Stokes computations of the present study are seen to be consistent with this conclusion.

A second contribution of Kluwick (1994) is that he delineated the appropriate form of the scaling laws for arbitrary, rather than perfect, gases. In particular, all of the perfect gas scalings carry over immediately to the case of arbitrary gases provided only that the pressure is expressed in terms of the pressure coefficient

$$c_p \equiv \frac{P - P_1}{\frac{1}{2}\rho_1 a_1^2 M_1^2}\ , \tag{1.3}$$

where M is the Mach number and the subscript 1 denotes the freestream conditions, and that the wall shear $\tau_{yx}\big|_w$ stress is expressed in terms of the skin friction coefficient

$$c_f = \frac{\tau_{yx}\big|_w}{\frac{1}{2}\rho_1 a_1^2 M_1^2}\ . \tag{1.4}$$

As an example, we note that the pressure distribution in the interaction region can be written

$$c_p \equiv \frac{\sqrt{c_{f1}}}{\sqrt[4]{M_1^2-1}}\tilde{P}(\tilde{x}) , \tag{1.5}$$

where c_{f1} is the skin friction immediately upstream of the interaction region and $\tilde{P}(\tilde{x})$ is the same function of the scaled x-variable $\tilde{x}$ as is found in the classical, i.e., perfect gas, theory.

An important parameter in any study of shock-boundary layer interaction is the overall pressure rise required for separation. Here we combine the estimate of Katzer (1989) with scaling laws of Kluwick (1994) to obtain

$$\frac{c_{pT}\sqrt[4]{M_1^2-1}}{\sqrt{c_{f1}}} > 2.6 \tag{1.6}$$

as the criterion for separation. Here c_{pT} is the pressure coefficient associated with the total pressure rise resulting from the reflection. As pointed out by Katzer (1989) the numerical factor on the right hand side of (1.6) can vary from author to author in the general range of 2 to 3. As an example we consider the shock-boundary layer interaction corresponding to Figure 1.3. The above ratio was found to be

$$\frac{c_{pT}\sqrt[4]{M_1^2-1}}{\sqrt{c_{f1}}} \approx 4.02$$

which is consistent with the criterion (1.6).

The same physics which causes the disintegration of compression discontinuities in $\Gamma<0$ fluids also gives rise to the formation of expansion shocks. A natural question

when considering the use of BZT fluids in applications is whether such expansion shocks can have deleterious effects upon interaction with boundary layers. Kluwick (1994) has also addressed this issue in the context of the triple-deck theory. His conclusions were that the interaction should resemble that of the perfect gas theory of expansion corners. As a result, expansion shocks will also not increase the likelihood of separation. In the present study we provide verification for this claim through use of our Navier-Stokes code.

The Navier-Stokes equations, boundary conditions and problem statement are given in Chapter 2. The gas models and physical data are discussed in Chapter 3. The implementation of the Beam and Warming scheme for dense gases is outlined in Chapter 4. Consistency checks on this implementation are also presented in this chapter.

Chapter 2

Formulation

In the present study, we restrict our attention to steady, two-dimensional flow of a Navier-Stokes fluid. Body forces and heat sources will be neglected and the flow is regarded as being single-phase and in equilibrium. The x and y coordinate axes are depicted in Figure 2.1. The origin is taken to be at some arbitrary distance x_0 upstream of the flat plate, the positive x axis is in the direction of the undisturbed flow, and the y direction is transverse to the incoming flow.

In the implementation of the numerical scheme described in Chapter 4, the unsteady form of the Navier-Stokes equations will be required. When these equations are written in conservation-law form, we have

$$\frac{\partial U}{\partial t}+\frac{\partial E_i}{\partial x}+\frac{\partial F_i}{\partial y}=\frac{\partial E_v}{\partial x}+\frac{\partial F_v}{\partial y}\ , \tag{2.1}$$

where

$$U = \begin{Bmatrix} \rho \\ \rho u \\ \rho v \\ E_t \end{Bmatrix}, \quad E_i = \begin{Bmatrix} \rho u \\ \rho u^2 + P \\ \rho uv \\ u(E_t + P) \end{Bmatrix}, \quad F_i = \begin{Bmatrix} \rho v \\ \rho uv \\ \rho v^2 + P \\ v(E_t + P) \end{Bmatrix}, \tag{2.2}$$

and

$$E_v = \begin{Bmatrix} 0 \\ \tau_{xx} \\ \tau_{yx} \\ w_x \end{Bmatrix}, \qquad F_v = \begin{Bmatrix} 0 \\ \tau_{xy} \\ \tau_{yy} \\ w_y \end{Bmatrix}. \tag{2.3}$$

The quantities u and v are the x and y components of the fluid velocity, P and ρ are the fluid pressure and density, and

$$E_t \equiv \rho(e + \frac{1}{2}(u^2 + v^2)) . \tag{2.4}$$

Here the thermodynamic quantity e is the thermal energy; thus, (2.4) will be referred to as the total energy per unit volume. The quantities τ_{xx}, τ_{xy}, τ_{yx}, and τ_{yy}, are the Cartesian components of the viscous part of the Navier-Stokes stress tensor which can be written

$$\tau_{xy} = \tau_{yx} = \mu(\frac{\partial u}{\partial y} + \frac{\partial v}{\partial x}) \quad ,$$

$$\tau_{xx} = (2\mu + \lambda)\frac{\partial u}{\partial x} + \lambda\frac{\partial v}{\partial y} \quad ,$$

$$\tau_{yy} = \lambda\frac{\partial u}{\partial x} + (2\mu + \lambda)\frac{\partial v}{\partial y} \quad , \tag{2.5}$$

where μ and λ are the shear and second viscosities which satisfy

$$\mu \geq 0, \ \mu_b = \lambda + \frac{2}{3}\mu \geq 0, \tag{2.6}$$

where μ_b is the bulk viscosity. The quantities w_x and w_y are the energy fluxes defined as

$$w_x \equiv u\tau_{xx} + v\tau_{xy} - q_x ,$$
$$w_y \equiv u\tau_{yx} + v\tau_{yy} - q_y , \tag{2.7}$$

where

$$q \equiv -k\nabla T$$

is the Fourier heat flux vector, T is the absolute temperature, and

$$k > 0 \tag{2.8}$$

is the thermal conductivity. The two terms in each of (2.7) represent the work done per unit time by the stress tensor. The first row of (2.1) is recognized as the mass equation, the second and third rows are the two components of the momentum equation, and the fourth row is the energy equation.

The plate is taken to be adiabatic, impenetrable, and located at $y=0, \ x > x_0$, where x_0 is the location of the leading edge of the plate. As a result, the physical boundary conditions at the plate can be written

$$u = v = \frac{\partial T}{\partial y} = 0 \text{ for } y=0, \ x > x_0 \ . \tag{2.9}$$

The flow far upstream, i.e., as $x \rightarrow -\infty$, is taken to be uniform with velocity components $u = u_1 > 0, \ v = 0$. The flow velocity u_1 is such that the incoming flow is

supersonic. Here we restrict our attention to reflections which leave the flow supersonic; thus, for the present purposes, Mach reflections will be ignored.

Chapter 3

Gas Models

A full specification of any single-phase gas requires a knowledge of the functions

$$P = P(\rho, T) , \qquad c_{v\infty} = c_{v\infty}(T) \tag{3.1}$$

and

$$\mu = \mu(\rho, T), \ \lambda = \lambda(\rho, T), \ k = k(\rho, T), \tag{3.2}$$

where $c_{v\infty}(T)$ is the low-pressure, i.e., the ideal gas, specific heat at constant volume. In the usual way we will refer to the first of (3.1) as the equation of state. In the present investigation we employ the equation of state proposed by Martin and Hou (1955). The advantage of this model is that it is widely employed in engineering practice and it has a strong analytical basis so that only a minimum number of experimental parameters are

required for its use. The Martin-Hou equation agrees well with the measured properties of light substances such as nitrogen and steam. Good agreement is also found when comparisons can be made to the heavier fluids of interest in studies of BZT fluids. The work of Thompson and Lambrakis (1973) and Cramer (1989) have also shown that it appears to be conservative with respect to predictions of negative nonlinearity. Details of the implementation of the Martin-Hou equation can be found in the articles by Martin and Hou (1955) and Cramer (1989).

The ideal gas specific heat will be modeled by a power-law of the form

$$c_{v_\infty}(T) = c_{v_\infty}(T_{ref})\left(\frac{T}{T_{ref}}\right)^n , \tag{3.3}$$

where T_{ref} is a reference temperature, and n is a material-dependent exponent. The advantage of (3.3) is its simplicity and accuracy over the temperature ranges of interest in the present study. The values of $c_{v_\infty}(T_{ref})$ and n are typically estimated by fitting (3.3) to empirical data or more complex models. Details of the fitting procedure for the heavier fluorocarbons are described by Cramer (1989).

Once the temperature dependence of the ideal gas specific heat and the full form of the equation of state (3.1) are known, all other thermodynamic parameters can be determined through use of the standard identities found in most texts on thermodynamics.

In the dense gas regime, the variation of the transport properties (3.2) with both density and temperature will be important. In the present investigation we employ the dense-gas shear viscosity and thermal conductivity models developed by Chung, et al. (1984, 1988). The key characteristics of these models are similar to the Martin-Hou

equation. That is, they have a strong analytical basis and therefore require only a minimum amount of physical data, and they reduce to standard ideal gas formulas in the low pressure limit. Furthermore, the comparisons provided by Reid, et al. (1987) reveal reasonable accuracy in the dense gas regime.

Finally, the bulk viscosity (2.6) must be specified. The authors know of no bulk viscosity data for light fluids in their high-pressure regime much less appropriate data for the heavier hydro- and fluorocarbons of interest here. Throughout, we will simply take the ratio μ_b/μ to be a numerical constant. It should be noted that errors in the value of the bulk viscosity are not likely to have a significant effect on the results. In the lowest order approximation of the boundary layer, the viscous-inviscid interaction region (as described by triple-deck theory), and the inviscid flow, the bulk viscosity is known to be negligible. The only influence of μ_b is expected to be in the description of the interior of shock waves. Numerical trials have verified that reasonable variations in the value of μ_b have essentially no effect on the complete inviscid-viscous interaction.

In order to ensure that the flow is single-phase, the final pressures and temperatures were checked against the Riedel (1954) vapor-pressure correlation. If any point was found to be in the two-phase regime, the whole calculation was rejected.

As pointed out above, each model for the equation of state, ideal gas specific heat, transport properties, and the phase boundary requires only a minimum number of physical data. The required quantities include the values of the pressure, temperature, and specific volume at the thermodynamic critical point, the boiling temperature, the molecular weight, the acentric factor and the dipole moment of the molecule. The acentric factor is a macroscopic measure of the acentricity of the molecule and is zero for spherical molecules such as those of monatomic gases. The definition of this factor may be found in Reid, et al. (1987) which reveals that it may be computed directly from

vapor-pressure data and the critical properties. The dipole moment is a measure of the polarity of the molecule and is zero for nonpolar substances. When polar substances such as steam, ammonia, acids, alcohols, and freons are considered, two more empirical constants are required. These are discussed below when the modeling of steam is considered.

The main Navier-Stokes computations described in Chapters 1, 4 and 5 involve air at low pressure, steam, N_2, SF_6, CO_2, PP11($C_{14}F_{24}$), and FC-71 (C_{18} $F_{39}N$). In the remainder of this section, we summarize the basis for the choices of the relevant physical parameters. The actual numerical values are tabulated in Table 3.1.

Most of the data for air was taken from Rohsenow, et al. (1985). The dipole moment was taken to be zero and the acentric factor was estimated to be identical to that of nitrogen; the value used was 0.039. The bulk viscosity was taken to be $0.6\,\mu$ as suggested by Truesdell (1953). Because the specific heat of air is nearly constant over a wide range of temperatures, we have taken n=0 in the calculations involving air in Chapters 1 and 4.

The physical data for steam is also well-established. Most of the relevant parameters were taken or estimated from those provided by Jones and Hawkins (1986) and Reid, et al. (1987). Because water is a polar substance, the shear viscosity and thermal conductivity models of Chung et al. (1984, 1988) require a so-called association factor and a second parameter related to the self-diffusion coefficient of water. Both parameters were chosen to be the values given by Chung et al. (1984) in their Tables I and III. No data for the bulk viscosity of water vapor is available at either low or high pressure. Here we simply set the ratio $\mu_b/\mu = 1$. Specific tests conducted in the present study show negligible variation in the resultant skin friction, wall pressure, and

wall temperature as μ_b is ranged from 0 to 5μ. A comparison plot of the skin friction is shown in Figure 3.1.

The bulk of the data for the heat transfer fluids FC-71 and PP11 were taken or estimated from the manufacturers' (3-M Corporation and Imperial Smelting Corporation) technical publications. A detailed discussion of the estimation procedures and results for the critical properties, boiling temperature, and specific heat data is found in the article by Cramer (1989). Private communication between Professor M. S. Cramer with the manufacturers' representatives indicates that PP11 and FC-71 are nonpolar so that the dipole moment was taken to be zero for each fluid. No data for the bulk viscosity of either PP11 or FC-71 exists and we took $\mu_b = 5\mu$ for each fluid.

In our checks on the numerical scheme we also employed N_2, CO_2 and SF_6. In each case the bulk of the data was taken from that provided by Reid, et al. (1987). The bulk viscosity for N_2 was taken to be that of air, i.e., 0.6μ. Truesdell (1953) and Emanuel and Argrow (1994) have pointed out that many authors have estimated the bulk viscosity of CO_2 to be on the order of $10^3\mu$. Furthermore, Emanuel and Argrow (1994) estimate the bulk viscosity of SF_6 to be 315μ. However, preliminary numerical computations and some theoretical analysis by Professor M. S. Cramer have indicated that the scaling laws associated with classical triple-deck theory may break down when the bulk viscosity is large compared to the shear viscosity. These discoveries complement those of Emanuel (1992) who predicted that even the ordinary boundary layer approximation may break down when both the Mach number and μ_b/μ are large. Thus, for the purposes of checking the numerical scheme against the classical scaling laws we will simply employ relatively low values of μ_b for both CO_2 and SF_6. In the case of SF_6 we used $\mu_b = 2\mu$ and in the case of CO_2 we used values of 0 and 100μ.

Further details of the potential breakdown in the scaling laws will be provided in future publications.

Chapter 4

Numerical Scheme

The Navier-Stokes equations (2.1)-(2.7) are solved by the well-known Beam-Warming implicit scheme (1976, 1978) adapted to allow for the dense gas equation of state and transport laws. The algorithm is second-order-time accurate, noniterative, and spatially factored. Explicit second and fourth-order artificial viscosities were added to reduce oscillations at the shocks. The advantage of this scheme is that it is well-known and can be immediately extended to imperfect gases. Full details of its implementation in the present application and the nondimensionalization scheme are given below.

To minimize the computation time without sacrificing accuracy, a grid, clustered in the direction transverse to the plate, was employed. The mapping between the physical and computational domain is given by

$$\frac{\xi}{L} = \frac{x}{L}, \qquad \frac{\eta}{H} = 1 - \frac{\ln\left[\frac{\beta+1-y/H}{\beta-1+y/H}\right]}{\ln\left[\frac{\beta+1}{\beta-1}\right]}, \tag{4.1}$$

where $\bar{\xi} = \xi/L = \xi(x)/L = \bar{x} = x/L$, $\bar{\eta} = \eta/H = \eta(y)/H$, and $\bar{y} = y/H$ are the nondimensional computational variables, β is the clustering parameter satisfying the condition $\beta>1$, and L and H are the dimensions of the computation domain in the flow and transverse directions, respectively. Typical values of β were between 1.002 and 1.003. As a result, the number of points across the boundary layer at the shock impingement point was approximately 20-40. The clustered grid system (21 by 21) is shown in Figure 4.1. The Jacobian for the transformation is

$$J = \eta_y = \frac{2\beta}{\left[\beta^2 - (1-\bar{y})^2 y\right] \ln\left[\frac{\beta+1}{\beta-1}\right]}, \tag{4.2}$$

where

$$\bar{y} = \frac{\beta+1+(1-\beta)\left[\frac{\beta+1}{\beta-1}\right]^{1-\bar{\eta}}}{\left[\frac{\beta+1}{\beta-1}\right]^{1-\bar{\eta}}+1}. \tag{4.3}$$

Once the mapping (4.1) is applied to the Navier-Stokes equations (2.1)-(2.3), we find that these equations can be rewritten as :

$$\frac{\partial}{\partial t}\left(\frac{\rho}{J}\right) + \frac{\partial}{\partial \xi}\left(\frac{\rho u}{J}\right) + \frac{\partial}{\partial \eta}(\rho v) = 0, \tag{4.4}$$

$$\frac{\partial}{\partial t}\left(\frac{\rho u}{J}\right) + \frac{\partial}{\partial \xi}\left(\frac{\rho u^2 + P - \tau_{xx}}{J}\right) + \frac{\partial}{\partial \eta}(\rho uv - \tau_{xy}) = 0, \tag{4.5}$$

$$\frac{\partial}{\partial t}\left(\frac{\rho v}{J}\right)+\frac{\partial}{\partial \xi}\left(\frac{\rho uv-\tau_{xy}}{J}\right)+\frac{\partial}{\partial \eta}(\rho v^2+P-\tau_{yy})=0\ , \tag{4.6}$$

$$\frac{\partial}{\partial t}\left(\frac{E_t}{J}\right)+\frac{\partial}{\partial \xi}\left(\frac{(E_t+P)u-u\tau_{xx}-v\tau_{xy}+q_x}{J}\right)+\frac{\partial}{\partial \eta}((E_t+P)v-u\tau_{xy}-v\tau_{yy}+q_y)=0\ . \tag{4.7}$$

An equivalent but more compact form is

$$\frac{\partial}{\partial t}\left(\frac{U}{J}\right)+\frac{\partial}{\partial \xi}\left(\frac{E_i}{J}\right)+\frac{\partial}{\partial \eta}(F_i)=\frac{\partial}{\partial \xi}\left(\frac{E_v}{J}\right)+\frac{\partial}{\partial \eta}(F_v)\ , \tag{4.8}$$

where U, E_i, F_i, E_v, F_v, and E_t have been defined in (2.2) to (2.3).
The stress tensor and Fourier heat flux vector can be rewritten in the new coordinate system as

$$\begin{aligned}
\tau_{xy}&=\tau_{yx}=\mu\left(\frac{\partial u}{\partial \eta}\eta_y+\frac{\partial v}{\partial \xi}\right),\\
\tau_{xx}&=(2\mu+\lambda)\frac{\partial u}{\partial \xi}+\lambda\frac{\partial v}{\partial \eta}\eta_y\ ,\\
\tau_{yy}&=\lambda\frac{\partial u}{\partial \xi}+(2\mu+\lambda)\frac{\partial v}{\partial \eta}\eta_y\ ,
\end{aligned} \tag{4.9}$$

$$\begin{aligned}
q_x&=-k\frac{\partial T}{\partial \xi}\ ,\\
q_y&=-k\frac{\partial T}{\partial \eta}\eta_y\ .
\end{aligned} \tag{4.10}$$

Furthermore, if we split $E_v=V_1+V_2$ and $F_v=W_1+W_2$, where V_1 and W_1 contain ξ derivatives only, and V_2 and W_2 contain η derivatives only, then we can rewrite (4.8) as :

$$\frac{\partial}{\partial t}\left(\frac{U}{J}\right)+\frac{\partial}{\partial \xi}\left(\frac{E_i}{J}\right)+\frac{\partial}{\partial \eta}(F_i)=\frac{\partial}{\partial \xi}\left(\frac{V_1}{J}\right)+\frac{\partial}{\partial \xi}\left(\frac{V_2}{J}\right)+\frac{\partial}{\partial \eta}(W_1)+\frac{\partial}{\partial \eta}(W_2)\ . \tag{4.11}$$

In the following scaling process of normalization, the subscripts ∞ , c, and the superscript $*$ denote, respectively, the free stream condition, the thermodynamic critical-point condition, and the reference condition of low-pressure versions evaluated at a reference temperature equal to the thermodynamic critical temperature T_c and at a reference pressure of one atmosphere. L and H are the dimensions of the computation domain in the flow and transverse directions, respectively. Then symbolically we can write

$$\bar{u}=u/u_1,\quad \bar{v}=v/u_1,\quad \bar{P}=P/P_c,\quad \bar{\rho}=\rho/\rho_C, \tag{4.12}$$

$$\bar{T}=T/T_C,\quad \bar{\mu}=\mu/\mu^*,\quad \bar{\lambda}=\lambda/\mu^*,\quad \bar{k}=k/k^*, \tag{4.13}$$

$$\bar{t}=tU_\infty/L,\quad \bar{e}=e/RT_c,\quad \bar{a}=a/\sqrt{RT_c},$$

$$\overline{E_t}=E_t/\rho_c RT_c,\quad \overline{C_p}=C_p/C_{p\infty}^*. \tag{4.14}$$

Then the nondimensionalized Navier-stokes equations can be rewritten as :

$$\frac{\partial}{\partial \bar{t}}\left(\frac{\bar{\rho}}{\hat{J}}\right)+\frac{\partial}{\partial \bar{\xi}}\left(\frac{\bar{\rho}\bar{u}}{\hat{J}}\right)+\frac{\partial}{\partial \bar{\eta}}(\bar{\rho}\bar{v})=0\quad , \tag{4.15}$$

$$\begin{aligned}&\frac{\partial}{\partial \bar{t}}\left(\frac{\bar{\rho}\bar{u}}{\hat{J}}\right)+\frac{\partial}{\partial \bar{\xi}}\frac{1}{\hat{J}}\left[\bar{\rho}\bar{u}^2+Z\bar{P}-2\Re\bar{\mu}\frac{\partial \bar{u}}{\partial \bar{\xi}}-\Re\bar{\lambda}\left(\frac{\partial \bar{u}}{\partial \bar{\xi}}+\hat{J}\frac{\partial \bar{v}}{\partial \bar{\eta}}\right)\right]\\&+\frac{\partial}{\partial \bar{\eta}}\left[\bar{\rho}\bar{u}\bar{v}-\Re\bar{\mu}\left(\hat{J}\frac{\partial \bar{u}}{\partial \bar{\eta}}+\frac{\partial \bar{v}}{\partial \bar{\xi}}\right)\right]=0\quad ,\end{aligned} \tag{4.16}$$

$$\frac{\partial}{\partial \bar{t}}\left(\frac{\bar{\rho}\bar{v}}{\hat{J}}\right)+\frac{\partial}{\partial \bar{\xi}}\frac{1}{\hat{J}}\left[\bar{\rho}\bar{u}\bar{v}\ -\Re\bar{\mu}\left(\hat{J}\frac{\partial \bar{u}}{\partial \bar{\eta}}+\frac{\partial \bar{v}}{\partial \bar{\xi}}\right)\right]$$
$$+\frac{\partial}{\partial \bar{\eta}}\left[\bar{\rho}\bar{v}^2+Z\bar{P}-\Re\bar{\lambda}\left(\frac{\partial \bar{u}}{\partial \bar{\xi}}+\hat{J}\frac{\partial \bar{v}}{\partial \bar{\eta}}\right)-2\Re\bar{\mu}\hat{J}\frac{\partial \bar{v}}{\partial \bar{\eta}}\right]=0\ , \tag{4.17}$$

$$\frac{\partial}{\partial \bar{t}}\left(\frac{\bar{E}_t}{\hat{J}}\right)+\frac{\partial}{\partial \bar{\xi}}\frac{1}{\hat{J}}\left[(\bar{E}_t+Z_c\bar{P})\bar{u}-\bar{u}\left(2\hat{R}\bar{\mu}\frac{\partial \bar{u}}{\partial \bar{\xi}}+\hat{R}\bar{\lambda}\left(\frac{\partial \bar{u}}{\partial \bar{\xi}}+\hat{J}\frac{\partial \bar{v}}{\partial \bar{\eta}}\right)\right)\right.$$
$$\left.-\bar{v}\left(\hat{R}\bar{\mu}\left(\hat{J}\frac{\partial \bar{u}}{\partial \bar{\eta}}+\frac{\partial \bar{v}}{\partial \bar{\xi}}\right)\right)-D\hat{k}\frac{\partial \bar{T}}{\partial \bar{\xi}}\right]$$
$$+\frac{\partial}{\partial \bar{\eta}}\left[(\bar{E}_t+Z_c\bar{P})\bar{v}-\bar{u}\left(\hat{R}\bar{\mu}\left(\hat{J}\frac{\partial \bar{u}}{\partial \bar{\eta}}+\frac{\partial \bar{v}}{\partial \bar{\xi}}\right)\right)-\bar{v}\left(\hat{R}\bar{\lambda}\left(\frac{\partial \bar{u}}{\partial \bar{\xi}}+\hat{J}\frac{\partial \bar{v}}{\partial \bar{\eta}}\right)\right.\right. \tag{4.18}$$
$$\left.\left.+2\hat{R}\bar{\mu}\hat{J}\frac{\partial \bar{v}}{\partial \bar{\eta}}\right)-D\bar{k}\hat{J}\frac{\partial \bar{T}}{\partial \bar{\eta}}\right]=0\quad ,$$

where

$$\hat{J}=\frac{L}{H}J\ , \tag{4.19}$$

$$Z_c=\frac{P_c}{\rho_c R T_c}\ , \tag{4.20a}$$

$$Z=\frac{P_c}{\rho_c u_1^2}=\frac{P_c}{\rho_c R T_c}\frac{RT_c}{u_1^2}=Z_c Z_r{}^2 \text{ with } Z_r{}^2=\frac{RT_c}{u_1^2}\ , \tag{4.20b}$$

$$\Re=\frac{\mu^*}{\rho_c u_1 L}=\frac{\bar{\rho}_1}{\bar{\mu}_1 Re_1}\ , \tag{4.21}$$

$$Re_1 = \frac{u_1 L \rho_1}{\mu_1} \quad = \text{Reynolds number based on the characteristic length of } L \,, \qquad (4..22)$$

$$\hat{R} = \frac{\mu^* u_1}{\rho_e R T_e L} = \frac{\Re u_1^2}{R T_e} = \frac{\overline{\rho}_1}{\overline{\mu}_1} \frac{1}{Re_1} \frac{1}{Z_r^{\,2}} = \frac{\Re}{Z_r^{\,2}} \,,$$

$$D = \frac{k^*}{\rho_e R u_1 L} = \frac{\overline{\rho}_1}{\overline{k}_1} \frac{\overline{C}_{p1}}{\Pr_1 \delta Re_1}, \quad \delta = \frac{R}{C^*_{p\infty}} \,. \qquad (4.23)$$

The shear stress τ_{xy} becomes:

$$\begin{aligned}
\tau_{xy} &= \tau_{yx} = \mu\left(\frac{\partial u}{\partial \eta} J + \frac{\partial v}{\partial \xi}\right) \\
&= \mu^* \overline{\mu}\left(\frac{U_\infty}{h}\frac{\partial \overline{u}}{\partial \overline{\eta}} J + \frac{U_\infty}{L}\frac{\partial \overline{v}}{\partial \overline{\xi}}\right) \\
&= \frac{\mu U_\infty}{L}\left(\frac{L}{h}\frac{\partial \overline{u}}{\partial \overline{\eta}} J + \frac{\partial \overline{v}}{\partial \overline{\xi}}\right) = \frac{\mu U_\infty}{L}\left(\hat{J}\frac{\partial \overline{u}}{\partial \overline{\eta}} + \frac{\partial \overline{v}}{\partial \overline{\xi}}\right) \qquad (4.24) \\
&= R\frac{P_e}{Z}\overline{\mu}\left(\frac{\partial \overline{u}}{\partial \overline{\eta}}\hat{J} + \frac{\partial \overline{v}}{\partial \overline{\xi}}\right) \,.
\end{aligned}$$

Hence, the non-dimensional skin friction becomes

$$c_f = \frac{2\tau_{xy}\big|_{wall}}{\rho_1 u_1^2} = \frac{2}{\overline{\mu}_1 Re_1}\left[\overline{\mu}\left(\frac{\partial \overline{u}}{\partial \overline{\eta}}\hat{J} + \frac{\partial \overline{v}}{\partial \overline{\xi}}\right)\right]_{wall} = \frac{2}{\overline{\mu}_1 Re_1}\left[\overline{\mu}\frac{\partial \overline{u}}{\partial \overline{\eta}}\hat{J}\right]_{wall} \,. \qquad (4.25)$$

In a compact form, dropping the hats and the bars, the governing equations (4.15) through (4.18) can be rewritten as :

$$\frac{\partial}{\partial t}U + \frac{\partial}{\partial \xi}E_i + \frac{\partial}{\partial \eta}F_i = \frac{\partial}{\partial \xi}V_1 + \frac{\partial}{\partial \xi}V_2 + \frac{\partial}{\partial \eta}W_1 + \frac{\partial}{\partial \eta}W_2 \,, \qquad (4.26)$$

where

$$U = \frac{1}{J}\begin{Bmatrix} \rho \\ \rho u \\ \rho v \\ E_t \end{Bmatrix} = \begin{Bmatrix} U_1 \\ U_2 \\ U_3 \\ U_4 \end{Bmatrix}, \tag{4.27a}$$

$$E_i(U) = \frac{1}{J}\begin{Bmatrix} \rho u \\ \rho u^2 + ZP \\ \rho uv \\ u(E_t + Z_c P) \end{Bmatrix}, \qquad F_i(U) = \begin{Bmatrix} \rho v \\ \rho uv \\ \rho v^2 + ZP \\ v(E_t + Z_c P) \end{Bmatrix}, \tag{4.27b}$$

$$V_1(U, U_\xi) = \frac{1}{J}\begin{Bmatrix} 0 \\ \Re(2\mu + \lambda) u_\xi \\ \Re\mu\, v_\xi \\ \hat{R}(2\mu + \lambda) u u_\xi + \hat{R}\mu v v_\xi + DkT_\xi \end{Bmatrix}, \tag{4.28a}$$

$$V_2(U, U_\eta) = \begin{Bmatrix} 0 \\ \Re\lambda\, v_\eta \\ \Re\mu u_\eta \\ \hat{R}\lambda u v_\eta + \hat{R}\mu v u_\eta \end{Bmatrix}, \tag{4.28b}$$

$$W_1(U, U_\xi) = \begin{Bmatrix} 0 \\ \Re\mu\, v_\xi \\ \Re\lambda\, u_\xi \\ \hat{R}\mu u v_\xi + \hat{R}\lambda v u_\xi \end{Bmatrix}, \tag{4.29a}$$

and

$$W_2(U,U_\eta) = J\begin{Bmatrix} 0 \\ \Re\mu u_\eta \\ \Re(\lambda+2\mu)v_\eta \\ \hat{R}\mu uu_\eta + \hat{R}(\lambda+2\mu)vv_\eta + DkT_\eta \end{Bmatrix}. \qquad (4..29b)$$

If we rewrite the equations (4.26) in the delta form of the implicit factored scheme of Beam and Warming (1978), they take the form

$$\left\{[I]+\frac{\theta_1\Delta t}{1+\theta_2}\left[\frac{\partial}{\partial\xi}([A]-[P]+[R_\xi])^n-\frac{\partial^2}{\partial\xi^2}[R]^n+\frac{\partial}{\partial\xi}([B]-[Q]+[S_\eta])^n-\frac{\partial^2}{\partial\eta^2}[S]^n\right]\right\}\Delta^n U$$

$$=\frac{\Delta t}{1+\theta_2}\left[\frac{\partial}{\partial\xi}(-E+V_1+V_2)^n+\frac{\partial}{\partial\eta}(-F+W_1+W_2)^n\right]$$

$$+\frac{\theta_1\Delta t}{1+\theta_2}\left[\frac{\partial}{\partial\xi}(\Delta^{n-1}V_2)+\frac{\partial}{\partial\eta}(\Delta^{n-1}W_1)\right]$$

$$+\frac{\theta_2}{1+\theta_2}\Delta^{n-1}U+O\left[(\theta_1-\frac{1}{2}-\theta_2)(\Delta t)^2+(\Delta t)^3\right]\equiv RHS\ ,$$

(4.30)

where $\Delta^n U \equiv U^{n+1}-U^n$, $U^n = U(\xi,\eta,n\Delta t)$, $U^{n+1} = U(\xi,\eta,(n+1)\Delta t)$, $[I]$ is the identity matrix, and the superscript n denotes evaluation at $(\xi,\eta,n\Delta t)$. Further details can be found from Beam and Warming (1978), and Anderson, et al. (1984). Table 4.1 shows

the various schemes depending upon the values of the parameters θ_1 and θ_2. The scheme used here is the 3-point backward scheme with $\theta_1 = 1$ and $\theta_2 = 0.5$.

The approximate factorization idea of Beam and Warming is to approximate the left hand side of (4.30) by a separable operator product, whose approximation error is no greater than that of the spatial finite difference approximations being used. This results in

$$\left\{[I]+\frac{\theta_1\Delta t}{1+\theta_2}\left[\frac{\partial}{\partial\xi}([A]-[P]+[R_\xi])^n-\frac{\partial^2}{\partial\xi^2}[R]^n\right]\right\}$$
$$\left\{[I]+\frac{\theta_1\Delta t}{1+\theta_2}\left[\frac{\partial}{\partial\eta}([B]-[Q]+[S_\eta])^n-\frac{\partial^2}{\partial\eta^2}[S]^n\right]\right\}\Delta^n U = RHS \quad , \tag{4.31}$$

where

$$[A]=\left[\frac{\partial E_i}{\partial U}\right]=$$

$$\begin{bmatrix} 0 & 1 & 0 & 0 \\ -u^2+\frac{Z}{J}\frac{\partial P}{\partial U_1} & 2u+\frac{Z}{J}\frac{\partial P}{\partial U_2} & \frac{Z}{J}\frac{\partial P}{\partial U_3} & \frac{Z}{J}\frac{\partial P}{\partial U_4} \\ -uv & v & u & 0 \\ \frac{uZ_c}{J}\frac{\partial P}{\partial U_1}-(E_t+Z_cP)\frac{u}{\rho} & \frac{uZ_c}{J}\frac{\partial P}{\partial U_2}+(E_t+Z_cP)\frac{1}{\rho} & \frac{uZ_c}{J}\frac{\partial P}{\partial U_3} & (\frac{Z_c}{J}\frac{\partial P}{\partial U_4}+1)u \end{bmatrix},$$

(4.32)

$$[\boldsymbol{B}]=\left[\frac{\partial \boldsymbol{F}_i}{\partial \boldsymbol{U}}\right]=$$

$$\begin{bmatrix} 0 & 0 & J & 0 \\ -Juv & Jv & Ju & 0 \\ -Jv^2+Z\dfrac{\partial P}{\partial U_1} & Z\dfrac{\partial P}{\partial U_2} & 2Jv+Z\dfrac{\partial P}{\partial U_3} & Z\dfrac{\partial P}{\partial U_4} \\ vZ_c\dfrac{\partial P}{\partial U_1}-J(E_t+Z_cP)\dfrac{v}{\rho} & vZ_c\dfrac{\partial P}{\partial U_2} & vZ_c\dfrac{\partial P}{\partial U_3}+J(E_t+Z_cP)\dfrac{1}{\rho} & (J+Z_c\dfrac{\partial P}{\partial U_4})v \end{bmatrix},$$

(4.33)

and

$$\frac{\partial P}{\partial U_1}=\delta\frac{P_T}{C_V}\frac{1}{U_1^3}\left[-U_4U_1+\frac{U_2^2}{Z_r^{\,2}}+\frac{U_3^2}{Z_r^{\,2}}\right]+J\left[\frac{a^2}{Z_c}-\delta Z_cP\frac{P_T}{\rho^2C_V}\right], \tag{4.34a}$$

$$\frac{\partial P}{\partial U_2}=-\delta\frac{P_T}{C_V}\frac{U_2}{U_1^2}\frac{1}{Z_r^{\,2}}, \tag{4.34b}$$

$$\frac{\partial P}{\partial U_3}=-\delta\frac{P_T}{C_V}\frac{U_3}{U_1^2}\frac{1}{Z_r^{\,2}}, \tag{4.35a}$$

$$\frac{\partial P}{\partial U_4}=\delta\frac{P_T}{C_V}\frac{1}{U_1}, \tag{4.35b}$$

with $P_T=\left.\dfrac{\partial P}{\partial T}\right|_{\rho}$ (4.36)

and

$$[\boldsymbol{R}]=\left[\frac{\partial \boldsymbol{V}_1}{\partial \boldsymbol{U}_\xi}\right],\ \boldsymbol{U}_\xi=\frac{\partial \boldsymbol{U}}{\partial \xi},\ \boldsymbol{U}_\eta=\frac{\partial \boldsymbol{U}}{\partial \eta},\tag{4.37a}$$

$$[\boldsymbol{S}]=\left[\frac{\partial \boldsymbol{W}_2}{\partial \boldsymbol{U}_\eta}\right],\ \left[\boldsymbol{R}_\xi\right]=\left[\frac{\partial \boldsymbol{R}}{\partial \xi}\right],\tag{4.37b}$$

$$[\boldsymbol{P}]=\left[\frac{\partial \boldsymbol{V}_1}{\partial \boldsymbol{U}}\right],\ [\boldsymbol{Q}]=\left[\frac{\partial \boldsymbol{W}_2}{\partial \boldsymbol{U}}\right],\ [\boldsymbol{S}_\eta]=\left[\frac{\partial \boldsymbol{S}}{\partial \eta}\right].\tag{4.37c}$$

Now, if only the steady state solution is desired, Beam and Warming (1978), Hirsh(1990), and Tannehill et al.(1978) have suggested that all viscous terms on the left-hand side of the algorithm (i.e., [[$\boldsymbol{P}$], [$\boldsymbol{R}$], [$\boldsymbol{Q}$], [$\boldsymbol{S}$], [$\boldsymbol{R}_\xi$], and [$\boldsymbol{S}_\eta$]) can be set equal to zero provided that the positive implicit smoothing (ε_i>0) is retained.

Then the equations with implicit and explicit damping parameters can be simplified to:

$$\left[[\boldsymbol{I}]+\lambda_1\left(\bar{\delta}_\xi[\boldsymbol{A}]^n-\varepsilon_i\bar{\delta}_\xi{}^2\right)\right]\Delta^n\boldsymbol{U}^*=\boldsymbol{RHS}-\frac{\varepsilon_{e1}}{\boldsymbol{J}}\left(\bar{\delta}_\xi{}^4+\bar{\delta}_\eta{}^4\right)\boldsymbol{J}\boldsymbol{U}^n+\frac{\varepsilon_{e2}}{\boldsymbol{J}}\left(\bar{\delta}_\xi{}^2+\bar{\delta}_\eta{}^2\right)\boldsymbol{J}\boldsymbol{U}^n\ ,\tag{4.38}$$

$$\left[[\boldsymbol{I}]+\lambda_1\left(\bar{\delta}_\eta[\boldsymbol{B}]^n-\varepsilon_i\bar{\delta}_\eta{}^2\right)\right]\Delta^n\boldsymbol{U}=\Delta^n\boldsymbol{U}^*\ ,\tag{4.39}$$

$$\boldsymbol{U}^{n+1}=\boldsymbol{U}^n+\Delta^n\boldsymbol{U}\ ,\tag{4.40}$$

where

$$\bar{\delta}_\xi\boldsymbol{u}_{j,k}=\frac{\boldsymbol{u}_{j+1,k}-\boldsymbol{u}_{j-1,k}}{2\Delta\xi}\ ,\tag{4.41a}$$

$$\bar{\delta}_{\xi}^{\,2} u_{j,k} = \frac{u_{j+1,k} - 2u_{j,k} + u_{j-1,k}}{\Delta\xi^2} \quad , \tag{4.41b}$$

$$\bar{\delta}_{\xi}^{\,4} u_{j,k} = \frac{u_{j+2,k} - 4u_{j+1,k} + 6u_{j,k} - 4u_{j-1,k} + u_{j-2,k}}{\Delta\xi^4} \quad , \tag{4.41c}$$

$$\lambda_1 = \frac{\theta_1}{1+\theta_2}\Delta t \quad , \tag{4.42}$$

and

ε_i = implicit damping parameter,

ε_{e1} , ε_{e2} = explicit damping parameters .

ε_{e2} includes the terms like $\partial^2 P / \partial\xi^2$, MacCormack (1975), and ε_{e1} in turned off when ε_{e2} exceeds ε_{e1}. The details can be found in Pulliam (1986).

Once the shock boundary-layer interaction equations are written in discrete delta forms, (4.38) to (4.40), an iterative procedure is invoked to solve the equations. First all the primitive and conservative variables are initialized by using the solution from the oblique-shock flat plate interaction problem assuming inviscid flow. With known left-hand-side matrices and right-hand-side vectors, (4.38) can be solved (the ξ direction), then (4.39) can be solved (the η direction) with known left-hand-side matrices and right-hand-side vector ΔU^*. Then U^n is updated by $U^n + \Delta^n U$. This procedure will be repeated, with current values of all the variables, until a certain convergence criterion is satisfied. Essentially the steady state solution is approached as time $t \to \infty$.

The algorithm used to implement the iteration scheme is outlined below.

---

0. Choose gas model.

1. Read in the fluid data.

2. Determine the values of parameters (i.e., grid sizes, β, etc.).

3. Choose models of equations of state, viscosity, and thermal conductivity.

4. Read in solution data from inviscid solver.

5. Impose appropriate boundary conditions. Set $n=1$.

6. Evaluate the left-hand side matrix and right-hand side vector of (4.38) and (4.39). Equations of state, viscosity, and conductivity are invoked here.

7. Solve (4.38) for $\Delta^n U^*$ (ξ -sweep).

8. Solve (4.39) for $\Delta^n U$ (η -sweep).

9. Update U by $U^{n+1} = U^n + \Delta^n U$, set $n = n+1$.

10. If solution has converged, stop.

11. Go to 6 with updated conservative variables and primitive variables. (Here, with the previous known value of U_4 (energy), Newton's method is necessary to find a new temperature as an input to the equation of state and others.).

The computational domain is depicted in Figure 2.1. The shock was introduced either at the inflow boundary (x=0) or at the upper boundary (y= H). At each of these boundaries, the flow variables were fixed at either the freestream conditions or the conditions after the incident shock; the latter conditions were computed from an iterative solution to the oblique shock relations similar to those described by Cramer (1991b). At the right boundary, outflow conditions were imposed. At the lower boundary (y=0), either symmetry conditions or the physical boundary conditions were applied as appropriate.

Extensive numerical checks and comparisons with known solutions have been carried out. A comparison of the results of our computations with the experimental data of Hakkinen, et al. (1959) is presented in Figure 4.2. The computed results of MacCormack (1982), Zhong(1994), and Walters (private communication, 1994) are also included. The freestream conditions, and shock pressure rise are listed in Table 4.2. The grid size employed by each investigator is also reported. Inspection of Figure 4.2 reveals reasonable agreement of our computations with those of previous authors. The calculated length of the separation region is overestimated considerably and Katzer (1989) argues that the Stanton probe contacting the wall could have influenced the length of the separation bubble. The skin friction of the numerical calculations behind the separation region is lower than that of experiment, which is also predicted by other calculations such as those of Pan and Cheng (1993), Katzer (1989), Ng et al. (1989), Thomas and Walters (1985), and Wagner and Schmidt (1978). Because the freestream pressures are on the order of one atmosphere or less, we regard these comparisons to be evidence that the dense-gas version of the Beam-Warming scheme recovers the perfect gas results in the low-pressure limit.

We have compared the results of the present scheme to the detailed computations of dense gas boundary layers reported by Whitlock (1992). In the latter studies a standard finite difference scheme was applied to the dense-gas version of the compressible boundary layer equations. Mach numbers ranging from zero to three and freestream pressures ranging from one atmosphere to slightly supercritical values were reported. Whitlock's results were found to be in excellent agreement with Anderson's (1991a) Navier-Stokes computations of compressible, dense-gas boundary layers on flat plates (private communication with Professor M. S. Cramer). The excellent agreement between our results and those of Whitlock is shown in Tables 4.3(a) and 4.3(b), which provide partial verification of the implementation of the numerical scheme and the dense-gas models.

We are not aware of any computations of the present kind which involve shock-boundary layer interactions in dense gases. The interactions presented by Wagner and Schmidt (1978) correspond to a freestream pressure of one bar. The Navier-Stokes computations of Anderson (1991a) involve transonic flow and nearly normal shocks on airfoils; as a result, no direct comparisons are appropriate. However, we have verified that the numerical scheme described here agrees well with the scaling laws of the dense-gas triple-deck theory developed by Kluwick (1994). The computed results for various fluids at various states are plotted in Figure 4.3; the corresponding flow data is recorded in Tables 4.4(a) and 4.4(b). We note that the cases included both low pressure and dense gas freestream conditions. In Figure 4.3, the local values of $\tilde{P}$ seen in (1.5) corresponding to separation (P_s) and the observed plateau (P_p) have been plotted as a function of the pressure ratio P_3 / P_1, i.e., the pressure ratio across the reflection as computed by the Navier-Stokes code. The plateau pressure was taken to be at the inflection point of the local pressure coefficient distribution. According to the dense-gas

scaling laws developed by Kluwick (1994), these values of P_s and P_p should be the same for every fluid and freestream condition. It was found that the average values of P_s and P_p were 1.39 and 2.31 approximately. Both values agree well with those of Katzer (1989) who based his estimates on computations employing air at low pressure. We also found slightly more scatter in the data for the plateau pressure than for the separation point. As discusssed by Katzer, the scatter tended to be largest where the separation was marginal. In fact, the worst case is the high-pressure calculation for N_2 which resulted in a separation region of only 4 grid points in the x direction. The separation was clearly marginal. Nevertheless, the value of P_s agrees reasonably well with that predicted in the low pressure computations. On the basis of these comparisons, we conclude that the dense-gas version of the Beam-Warming scheme is capable of describing the flows of interest in the present investigation.

Extensive tests were also made to determine the grid refinement required to render the computed results independent of the grid size. It was found that ξ vs. η grids in the range of 125 x 76 to 187 x 101, depending on the fluid, were adequate to ensure that the grid size no longer influenced the results, although even more refined grids were typically used. In any case, any comparisons were made using identical grids. It is expected, although not formally guaranteed, that any observed differences are due to the physics rather than differences in numerical error.

Chapter 5

Results

The first comparison to be made is that between steam and FC-71. The former fluid is chosen because it is a non-BZT fluid which is commonly employed in heat transfer and Rankine cycle applications. The latter fluid (FC-71) is a BZT fluid with a critical temperature approximately equal to that of steam. The following comparison will be direct in the sense that the behavior of both steam and FC-71 will be evaluated at equivalent flow conditions.

We first consider the flow of steam at a freestream pressure, temperature, and Mach number equal to 8.55 atm, 646.15 kelvins, and 2.0, respectively. The flow deflection angle carried by the incident shock was 3^0 and the position at which the incident shock strikes the plate corresponds to a local Reynolds number of 2.96×10^5. The computed skin friction and wall pressure coefficients are plotted in Figures 5.1-5.2. Inspection of Figure 5.1 reveals that the incident shock is strong enough to separate the

laminar boundary layer; in fact, the skin friction plot exhibits the classical double minimum profile suggesting that separation is well-established and not marginal.

We next consider the flow of the BZT fluid FC-71 at exactly the same freestream Mach number, pressure, and temperature. Furthermore, the flow deflection angle of the incident compression wave is also taken to be 3^0. Thus, the geometry generating the compression can be said to be identical for both fluids. Under these conditions the upstream and downstream values of the scaled fundamental derivative $\frac{\rho\Gamma}{a}$ are -0.04 and -0.16, respectively. The fundamental shock existence conditions described by Menikoff and Plohr (1989) and Cramer (1991a) can be employed to show that this compression discontinuity is inadmissible. Furthermore, it is easily verified that the original discontinuity will disintegrate into a centered isentropic compression fan. Because this compression wave arrives at the boundary layer with a nonzero width, the definition of the impingement Reynolds number must be reconsidered. In order to make a meaningful comparison, we choose the initiation point of the compression wave to be such that the local Reynolds number at the approximate center of the wave is equal to that used in the calculation involving steam, i.e., 2.96×10^5. The location of the wave impingement was estimated as that predicted by the numerical solution to the exact oblique shock relations for the inadmissible discontinuity. It is easily shown that the computed impingement point of the inadmissible shock will always lie between the impingement points of the first and last Mach waves of the actual centered fan, at least when $\Gamma < 0$ both upstream and downstream of the proposed discontinuity. In fact, weak shock theories of the type described by Cramer (1991a) and Crickenberger (1991) can be used to show that the inadmissible discontinuity always bisects the resultant centered fan. This result is recognized as the $\Gamma < 0$ counterpart of the bisection rule described in many texts on gasdynamics; see, e.g., Whitham (1974).

Inspection of Figures 5.1-5.2 reveals that the interaction of the centered fan in FC-71 results in an attached boundary layer. The minimum skin friction is seen to be approximately 3 x 10^{-4} whereas that for steam is seen to be approximately -5 x 10^{-4}. Coincidentally, this large difference in the minimum skin friction is approximately the same as that seen in the comparisons between the shock and the isentropic compression wave depicted in Figure 1.2. Numerous tests indicate that the grid sizes (218x101 for FC-71 and 156x101 for steam) used for each fluid are adequate to ensure that the results are independent of the grid. We therefore conclude that the observed suppression of separation is of physical rather than numerical origin.

The variation of the pressure coefficient plotted in Figure 5.2 shows that the total change in c_p during the reflection is slightly less than that of steam. This difference is due to the fact that the compression in FC-71 is isentropic whereas that in steam involves an increase in entropy. Similar differences between compression fans and compression shocks were seen in the Euler computations of Monaco (1994). When the separation parameter seen on the left of (1.6) is computed it is found that

$$\frac{c_{pT}\sqrt[4]{M_1^2-1}}{\sqrt{c_{f1}}} \approx 4.78$$

for steam and is

$$\approx 4.01$$

for FC-71. As expected, both values are well above those needed to produce separation. We also note that the value for FC-71 is approximately that recorded for the shock-induced separation seen in Figure 1.3.

In order to demonstrate that the advantageous behavior of FC-71 is associated with the novel dynamics associated with the $\Gamma < 0$ regime and is not due to the

particular choice of FC-71, we have computed a case where the freestream state of FC-71 corresponds to a nearly perfect gas. The freestream temperature, freestream Mach number, the flow deflection angle of the incident shock and the impingement Reynolds number were all taken to be identical to those of steam. The only difference between this case and that of the cases already discussed is that the freestream pressure was taken to be 1 atm instead of 8.55 atm. The values of $\frac{\rho\Gamma}{a}$ ahead of and behind the incident shock were both found to be approximately 1.0; this value is to be expected given large values of the ideal-gas specific heat of FC-71. As in the case of steam the resultant compression discontinuity can be shown to be admissible and arrives at the boundary layer as a discontinuity, at least according to the inviscid theory. The skin friction and wall pressure coefficient have been plotted in Figures 5.1-5.2. Because the incoming signal is now a shock and the scaled strength parameter

$$\frac{c_{pT}\sqrt[4]{M_1^2-1}}{\sqrt{c_{f1}}} \approx 4.76,$$

the boundary layer is seen to separate with approximately the same minimum pressure coefficient as obtained for steam. The main difference between the skin friction variations is the apparent width of the separation zone. However, this is due to the scaling of x with L_s. The latter was chosen to ensure that the impingement Reynolds numbers of steam and FC-71 were identical. Because the Mach numbers were also matched, the values of L_s will be different for different fluids. In particular, it is the differences in the factor $\frac{\mu}{\rho a}$ which cause the differences in L_s.

The results of this comparison give further evidence for the idea that the suppression of separation in FC-71 is due to the unique dynamics of BZT fluids in their $\Gamma < 0$ regime. A detailed inspection of the incoming boundary layer as well as similar

inspections of dense gas boundary layers computed by Whitlock (1992) reveal no unusual dynamics in the viscous flow regime. We therefore conclude that the main physical reason for the suppression of separation in BZT fluids is due to the nonzero width of the incoming compression wave which in turn is due to the disintegration of compression discontinuities in the $\Gamma < 0$ regime.

To further illustrate the effect of the width of the compression fan on the boundary layer we consider the flow of FC-71 at exactly the same freestream pressure (8.55 atm), temperature (646.15 kelvins) and Mach number (2.0) as used in our comparison between steam and FC-71. The initiation point of the compression discontinuity was chosen so that the approximate impingement Reynolds number was 2.96×10^5 and the transverse distance from the plate was identical to that used in the previous examples. The flow deflection angle of the incident wave was taken to be 6.5^0 instead of 3^0. The freestream value of $\frac{\rho\Gamma}{a}$ is of course identical to that of the previous example involving FC-71, i.e., -0.04, and the value of $\frac{\rho\Gamma}{a}$ after the discontinuity was form to be -0.06. As in the previous example, the discontinuity can be shown to be inadmissible; as a result it naturally disintegrates into a centered fan. The resultant skin friction and wall pressure coefficient variations are plotted in Figures 5.3-5.4. A plot of constant c_p contours in $(x/L,\ y/H)$ space is plotted in Figure 5.5(a). These contours are plotted at intervals of $\Delta c_p = 3.3 \times 10^{-3}$. Although the waves strikes the boundary layer as a fan, the overall compression is over twice as large as the strength of the previous example of a compression fan. As a result, the pressure rise is so large that the boundary layer separates.

It is of interest to note that the relation between the flow deflection angle $\tilde{\theta}$ carried by the incident fan and the incident wave strength and wave width (Δx)can be approximated by

$$c_{p2} \approx \frac{2\tilde{\theta}_2}{\sqrt{M_1^2 - 1}} \quad \text{and} \quad \Delta x \approx -\frac{M_1^4}{M_1^2 - 1} \frac{\rho_1 \Gamma_1}{a_1} \tilde{\theta}_2 \Delta y \tag{5.1}$$

where c_{p2} is the pressure coefficient immediately following the fan as estimated by the linear simple-wave theory and Δy is the distance between the initiation point of the fan and the plate measured transverse to the flow. The second of (5.1) can be obtained from a $\frac{\rho\Gamma}{a} = 0(1)$ version of the weak shock theory of Crickenberger (1991) or Cramer (1991a) or by a small disturbance approximation of Thompson's (1971) expression for the Mach angles in an isentropic simple wave:

$$\frac{d\psi}{d\tilde{\theta}} = \frac{\rho\Gamma}{a} \frac{M^2}{M^2 - 1},$$

where ψ is the exact (convected) Mach angle and M is the local Mach number. Thus, as the flow deflection angle increases, both the strength and width increase at approximately the same rate. A comparison of Figures 5.1 and 5.3 suggests that the effect of the increase in strength dominates that of the increase in width which in turn results in the observed flow separation.

To isolate the effect of the width of the incoming wave we have computed the flow of FC-71 under exactly the same freestream conditions and impingement Reynolds number with exactly the same inadmissible compression discontinuity. The only difference between this case and that just described is that the initiation point of the

compression discontinuity in the present case is located at a transverse distance which is 61% farther from the plate. As a result, the compression wave striking the plate boundary layer is 61% wider than that of the previous case. The results for the skin friction and wall pressure coefficient are plotted in Figures 5.3-5.4. The c_p contours are plotted in Figure 5.5(b) using c_p intervals which are identical to that used in Figure 5.5(a). Inspection of Figures 5.3-5.5 reveal that the increase in the initiation distance and therefore the increase in final wave width is sufficient to attach the flow. With respect to the task of isolating the effect of wave width, we regard the comparison seen in Figures 5.3-5.5 to be more direct than that between steam and FC-71 due to the fact that all parameters except the width were held fixed in the present case. In this sense the present comparison is closely related to that done for air in Chapter 1. Because all viscous effects are expected to be identical in the examples illustrated by Figures 5.3-5.5, the comparisons provide further strong evidence for the idea that the observed suppression of separation is caused by differences in the incoming signal which in turn is due to the unique inviscid dynamics of BZT fluids.

As a final example of shock boundary layer interaction in BZT fluids we consider the case of the collision of an expansion shock with a boundary layer. The fluid is PP11 at a freestream pressure, temperature and Mach number of 13.8 atm, 648.90 kelvins, and 2.0, respectively. The initiation point of the wave was taken to be such that impingement Reynolds number was 2.96×10^5. The flow deflection angle was taken to be -3^0 which is of course consistent with the generation of an expansion wave. The value of $\frac{\rho\Gamma}{a}$ in the freestream was -0.20 and the value immediately after the expansion discontinuity was found to be -0.12. Under these conditions it can be shown that this discontinuity is admissible and therefore propagates as a shock wave. The variation of the skin friction and wall pressure coefficient is plotted in Figures 5.6-5.8.

Inspection of the first of these figures reveals that the expansion shock causes the skin friction to increase in the interaction region. The observation that expansion shocks cause no difficulties with respect to separation is consistent with the remarks of Kluwick (1994) as well as reasoning based on the perfect gas theory.

A second example of the interaction of an admissible expansion shock with a laminar boundary layer in FC-71 is also shown in Figures 5.6-5.8. The freestream pressure, temperature and Mach number were taken to be 8.97 atm, 646.20 kelvins, and 2.0, respectively. The impingement Reynolds number was the same as the case for PP11. The value of $\frac{\rho\Gamma}{a}$ in the freestream was -0.27 and the value immediately after the expansion discontinuity was found to be -0.16. The results are completely consistent with those of PP11. The wall temperature plot shows a little deviation as shown in Figure 5.8.

Chapter 6

Summary

The primary goal of the present investigation was to examine viscous-inviscid interactions in BZT fluids. This was done by generating numerical solutions to the full Navier-Stokes equations for the well-understood benchmark problem of the reflection of an oblique shock from a laminar boundary layer on a flat plate. In this dissertation, the Beam-Warming scheme was generalized such that flows involving dense, i.e., high pressure, gases could be computed. The main result is the demonstration that the use of BZT fluids in the $\Gamma < 0$ regime can suppress boundary layer separation. The evidence presented here as well as the analytical work of Kluwick (1994) strongly suggests that the primary physical reason for this suppression is the disintegration of compression discontinuities at temperatures and pressures corresponding to $\Gamma < 0$. As a result, the incident compression wave is of nonzero width which represents a decrease in the adverse pressure gradient carried by the wave. If the decrease in the pressure gradient is

large enough for a given strength of the compression wave, the boundary layer is able to remain attached during the interaction. A similar elimination of separation was observed in our example involving a sequence of compression waves of increasing width depicted in Figures 1.1-1.2 Thus, the key to understanding the suppression mechanism is the nonclassical dynamics of BZT fluids in the inviscid portion of the flow.

An advantage of the discovery of the relatively simple physical mechanism is that the perfect gas intuition regarding the viscous-inviscid interaction can be carried over with little or no modification. The main effort to reduce the separation will therefore be to control the inviscid portion of the flow.

We have also verified Kluwick's (1994) prediction that the interaction of expansion shocks with boundary layers causes no new difficulties with respect to separation. This conclusion is consistent with the idea that the nonclassical physical effects are primarily observed in the inviscid part of the flow.

References

Anders, J. B., 1993, "Heavy gas wind-tunnel research at Langley Research Center," ASME Paper 93-FE-5.

Anderson, D. A., Tannehill J. C., and Pletcher, R. H., 1984, Computational Fluid Mechanics and Heat Transfer, Hemisphere Publication corporation, New York.

Anderson, W. K., 1991a, "Numerical Study of the Aerodynamic Effects of Sulfur Hexafluoride (SF6) as a Test Gas in Wind Tunnels," NASA TP-3086.

Anderson, W. K., 1991b, "Numerical Study on Using Sulfur Hexafluoride as a Test Gas in Wind Tunnels," AIAA J. , Vol 29, No. 12, pp. 2179-2180.

Bober, W., and Chow, W. L., 1990, "Nonideal isentropic gas flow through converging-diverging nozzles," Journal of Fluids Engineering, Vol. 112, pp. 455-460.

Beam, R. M., and Warming, R. F., 1978, "An Implicit Factored Scheme for the compressible Navier-Stokes Equations," AIAA J., Vol. 16, No. 4, pp. 393-402.

Beam, R. M., and Warming, R. F., 1976, "An Implicit Finite-Difference Algorithm for Hyperbolic Systems in Conservation Law Form" J. Comp. Phys., Vol. 22,. pp. 87-110.

Bethe, H. A., 1942, "The theory of shock waves for an arbitrary equations of state," Office Sci. Res. & Dev. Report No. 545.

Chung, T. H., Ajlan, M., Lee, L.L., and Starling, K. E., 1988, "Generalized Multiparameter Correlation for Nonpolar and Polar Fluid Transport Theories," Ind. Eng. Chem. Res., Vol. 27, pp. 671-679.

Chung, T. H., Lee, L.L., and Starling, K. E., 1984, "Application of Kinetic Gas Theories and Multiparameter Correlation for Prediction of Dilute Gas Viscosity and Thermal Conductivity," Ind. Eng. Chem. Fund., Vol. 23, No.23, pp. 8-13.

Cramer, M. S., 1989, "Negative nonlinearity in selected fluorocarbons," Physics of Fluids A, Vol. 1, No. 11, pp.1984-1987.

Cramer, M. S., 1991a, "Nonclassical dynamics of classical gases" Nonlinear Waves in Real Fluids, edited by A. Kluwick, Springer-Verlag, New York, pp. 91-145.

Cramer, M. S., 1991b, "On the Mach number variation in steady flows of dense hydrocarbons," Journal of Fluids Engineering, Vol. 113, pp. 675-680.

Cramer, M. S., and Best, L. M, 1991, "Steady , isentropic flows of dense gases," Physics of Fluids A. Vol. 3, pp. 219-226.

Cramer, M. S., and Crickenberger, A. B., 1992, "Prandtl-Meyer Function for Dense Gases," AIAA journal, Vol. 30, No. 2, pp. 561-564.

Crickenberger, A. B., 1991, "The Dynamics of Steady Supersonic Dense Gas Flows," M. S. Thesis, Virginia Polytechnic Institute and State University, Blacksburg, Virginia.

Dziedzic, W. M., Jones, S. C., Gould, D. C., and Petley, D. H., 1993, "Analytical comparison of convective heat transfer correlation in superscritical hydrogen," Journal of Thermophysics and Heat Transfer, Vol. 7, No. 3, pp.68-73.

Emanuel, G., and Argrow, B. M., 1994, "Linear dependence of the bulk viscosity on shock wave thickness," Physics of Fluids , Vol. 6 , No. 9, pp.3203-3205.

Emanuel, G., 1992, "Effect of bulk viscosity on the hypersonic boundary layer," Physics of Fluids A, Vol. 4, No. 3, pp.491-495.

Enkenhus, K. R., and Parazzoli, C., 1970, "Dense Gas Phenomena in a Free-Piston Hypersonic Wind Tunnel," AIAA Journal, Vol. 8, pp.60-65.

Hakkinen, R. J., Greber, I, and Trilling, L., 1959, "The interaction of an oblique shock wave with a laminar boundary ," NASA Memo 2-18-59W.

Hall, W, B., 1971, "Heat Transfer Near the Critical Point," article in Advances in Heat Transfer, ed. T. F. Irvine and J. P. Hartnett, Vol. 7, pp. 1-86.

Hirsch, C., 1990, Numerical Computation of Internal and External Flows, Vol I, II, John Wiley & Sons, New York.

Hsu, Y. Y., and Graham, R. W., 1976, Transport Processes in Boiling & Two-Phase Systems, Hemisphere Series in thermal and fluid engineering, McGraw-Hill, New York.

Jameson, A., et al. , 1981, "Numerical Solutions of the Euler Equations by Finite Volume Methods Using Runge-Kutta Time-Stepping Schemes," AIAA Paper 81-1259.

Jones, J. B., and Hawkins, G. A., 1972, Engineering Thermodynamics, McGraw-Hill, New York.

Katzer, E., 1989, "On the Scales of Laminar Shock/Boundary Layer Interaction," Journal of Fluid Mechanics, Vol. 206, pp. 477-496.

Kluwick, A., 1994, "Interacting laminar boundary layers of dense gases," Acta Mechanica, Springer-Verlag, Vol. 4, pp. 335-349.

Lambrakis, K., and Thompson, P. A., 1972, "Existence of real fluids with a negative fundamental derivative Γ," Physics of Fluids, Vol. 5, pp. 933-935.

Leung, J. C., and Epstein, M., 1988, "A generalized critical model for nonideal gases," AIChE Journal, Vol. 34, pp. 1568-1572.

MacCormack, R. W., and Baldwin, B. S, 1975, "A Numerical Method for Solving the Navier-stokes Equations with Application to Shock-Boundary Layer Interactions," AIAA Paper 75. Vol.1.

MacCormack, R. W., 1971, " Numerical solution of the interaction of a shock wave with a laminar boundary layer" Notes in Phys. 8, Berlin : Springer, pp. 151-163.

MacCormack, R. W., 1982, "A Numerical Method for Solving the Equations with of Compressible Viscous Flow," AIAA J., Vol. 20, No. 9, pp. 1275-1281.

Menikoff, R., and Plohr, B., 1989, "Riemann problem for fluid flow of real materials," Rev. Mod. Phys., .Vol. 61, pp. 75-130.

Martin, J. J., and Hou, Y. C., 1955, "Development of an Equation of State for Gases ," AIChE J., Vol. 1, No. 2, pp. 142-151.

Monaco, J. F, 1994, "Supersonic Flows of Bethe-Zel'dovich-Thompson Fluids in Cascade Configurations," M. S. Thesis, Virginia Polytechnic Institute and State University, Blacksburg, Virginia.

Ng, W. F., Mitchell, K., Ajmani, A. C., Taylor, III, and Brock, J. S., 1989, "Viscous Analysis of High Speed Flows Using An Upwind Finite Volume Technique.," AIAA, 27th Aerospace Science Meeting, Jan. 9-12, Reno, Nevada, pp. 1-8.

Pan, D., and Cheng, J-C, 1993, "Upwind Finite Volume Navier-stokes Computation on Unstructured Triangular Meshes." AIAA J., Vol.31, No.9, pp. 1618-1625.

Pulliam, Thomas H., 1986, "Artificial Dissipation Models for the Euler Equations" AIAA J., Vol.24, No.12, pp. 1931-1940.

Reid, R. C., Prausnitz, J. M., and Poling, B. E., 1987, The Properties of Gases & Liquids, 4th ed., McGraw-Hill, New York.

Reidel, L., 1954, " Eine neue Universelle Damfdruckformel-Untersuchungten über eine Erweiterung des Theorems der übereinstimmenden Zustände Teil 1," Chem. Ing. Tech., Vol. 26, pg. 83.

Reynolds, W. C., and Perkins, H. C., 1977, Engineering Thermodynamics, 2nd ed., McGraw-Hill, New York.

Rohsenow, W. M., Harnet, J. P., and Ganic E. N., 1985, Handbook of Heat Transfer Fundamentals, 2nd ed., McGraw-Hill, New York.

Schlichting, H., Boundary-Layer Theory, 7th ed., 1979, McGraw-Hill, New York.

Simeonides, G., 1987, "The Aerodynamic Design of Hypersonic Contoured Axisymmetric Nozzles Including Real Gas Effects," von Karman Institute for Fluid Dynamics Technical Memorandum 43.

Simeonides, G., 1990, "The VKI Hypersonic Wind Tunnels and Associated Measurement Techniques," von Karman Institute for Fluid Dynamics Technical Memorandum 46.

Tannehill, J., and Vigneron, Y., 1978, "Numerical solution of two-dimensional turbulent blunt body flows with an impinging shock," AIAA Paper 78-1209, pp. 1-15

Thomas, J. L., and Walters, R.W., 1985, "Upwind Relaxation Algorithms for the Navier-Stokes Equations," AIAA 7th Computational Fluid Dynamics Conference, July 15-17, Cincinnati, Ohio.

Thompson, P. A., 1971, "A fundamental derivative in gas dynamics," Physics of Fluids, Vol. 14, pp. 1843-1849.

Truesdell, C., 1953, "Precise Theory of the Absorption and Dispersion of Forced Plane Infinitesimal Waves according to the Navier-Stokes Equations," Journal of Rational Mechanics and Analysis, Vol. 2, pp. 643-741.

Thompson, P. A., and Lambrakis, K., 1973, "Negative shock waves" Journal of Fluid Mechanics, Vol. 16, pp. 187-208.

Wagner, B., and Schmidt, W., 1978, "Theoretical Investigations of Real Gas Effects in Cryogenic Wind Tunnels," AIAA J., Vol. 16, No. 6, pp. 580-586.

Walters, R. W., 1994, private communication.

Wendroff, B., 1972, "The Riemann problem for materials with nonconvex equations of state II: General flow," Journal of Math. Anal. Applics 38, pp. 640-658.

White, F. M., 1974, Viscous Fluid Flow, McGraw-Hill, New York.

Whitham, G. B., 1974, Linear and Nonlinear Waves, Wiley-Interscience, New York.

Whitlock, S. T., 1992, "Compressible Flows of Dense Gases in Boundary Layers," M. S. Thesis, Virginia Polytechnic Institue and State University, Blacksburg, Virginia.

Zel'dovich, Ya. B., 1946, "On the possibility of rarefaction shock waves," Zh. Eksp. Teor. 4, pg.363.

Zhong, X., 1994, "Application of Essentially Nonoscillatory Schemes to Unsteady Hypersonic Shock-Shock Interference Heating Problems," AIAA Journal, Vol. 32, No. 8, pp. 1606-1616.

Table 3.1 Properties of fluids used in this dissertation.

	Nitrogen	Air	Steam	CO_2
Molecular Weight	28.01	28.97	18.015	44.01
T_c (kelvins)	126.2	133.0	647.29	304.1
p_c (atm)	33.4	37.5	218	72.9
V_c (m^3/kg)	3.20E-3	3.21E-3	3.15E-3	2.13E-3
Z_c	0.29	0.32	0.233	0.274
T_b (kelvins)	77.4	80.0	373.15	194.7
Acentric Factor	0.039	0.039	0.344	0.239
$C_{p\infty}(T_c)/R$	2.589	2.5	3.448	3.501
n	0	0	0.225	0.526
Dipole Moment (debyes)	0	0	1.8	0
μ_b/μ	0.6	0.6	1	0-100
Beta*	-	-	1.282	-
Association Factor	-	-	0.076	-

* an empirical parameter related to the self-diffusion coefficient, Chung et al. (1984, 1988).

Table 3.1 Properties of fluids used in this dissertation, continued.

	SF_6	PP11	FC-71
Molecular Weight	146.05	624	971
T_C (kelvins)	318.7	650.15	646.15
P_C (atm)	37.11	14.41	9.3
V_C (m^3/kg)	1.36E-3	1.60E-3	1.62E-3
Z_C	0.282	0.2688	0.275
T_b (kelvins)	209.6	488.15	526.15
Acentric Factor	0.286	0.777	0.97
$C_{v\infty}(T_C)/R$	11.249	92.28	145.03
n	0.66	0.578	0.427
Dipole Moment (debyes)	0	0	0
μ_b/μ	2	5	5
Beta*	-	-	-
Association Factor	-	-	-

* an empirical parameter related to the self-diffusion coefficient, Chung et al. (1984, 1988).

Table 4.1 Numerical schemes for varous θ_1 and θ_2.

θ_1	θ_2	Scheme	Accuracy	for $U_t + f_x = 0$
0	0	Euler Explicit	$O(\Delta t)$	$\Delta U^n = -\Delta t \frac{\partial f^n}{\partial x^n}$
0	$-\frac{1}{2}$	Leapfrog Explicit	$O(\Delta t^2)$	$U^{n+1} - U^{n-1} = -2\Delta t \frac{\partial f^n}{\partial x^n}$
$\frac{1}{2}$	0	Trapaezoidal Implicit	$O(\Delta t^2)$	$(1 + \frac{\Delta t}{2}\frac{\partial A}{\partial x})\Delta U^n = -\Delta t \frac{\partial f^n}{\partial x^n}$
1	0	Euler Implicit	$O(\Delta t)$	$(1 + \Delta t \frac{\partial A}{\partial x})\Delta U^n = -\Delta t \frac{\partial f^n}{\partial x^n}$
1	$\frac{1}{2}$	3-Point Backward Implicit	$O(\Delta t^2)$	$(\frac{3}{2} + \Delta t \frac{\partial A}{\partial x})\Delta U^n = -\Delta t \frac{\partial f^n}{\partial x^n} + \frac{1}{2}\Delta U^{n-1}$

Table 4.2 Data of free stream conditons, pressure rise, and grids corresponding to Figure 4.2. The * in the last three references indicates that no explicit statement of the thermodynamic properties were given. However it is believed that these were at low pressure and room temperature.

Reference	P_1 (atm)	T_1 (kelvins)	M_1	P_3 / P_1	grid sizes
Present work	0.134	308.6	2	1.4	156x101
Walters (1994)	0.133	293	2	1.4	62x113
MacCormack (1982)	*	*	2	1.4	32x32
Zhong (1994)	*	*	2	1.4	102x144
Hakkinen et al. (1959)	*	*	2	1.4	N/A

Table 4.3(a) Comparison of the results for the skin friction as computed in the present work to those of S. T. Whitlock (1992) for a pure compressible boundary layer.

Fluid	M_1	T_1 (kelvins)	p_1 (atm)	$c_f / c_{f_{Blasius}}$ Present study	$c_f / c_{f_{Blasius}}$ Whitlock(1992)
N_2	2	127.5	1	0.980	0.983
N_2	2	127.5	31.6	0.770	0.775
N_2	2	127.5	36.2	0.560	0.533
N_2	3	127.5	1	0.945	0.950
N_2	3	127.5	31.6	0.7	0.7
SF_6	2	321.9	1	1	1
SF_6	2	321.9	35.3	0.88	0.90
SF_6	2	321.9	41.0	0.71	0.70

Table 4.3(b) Comparison of the results for the wall temperature as computed in the present work to those of S. T. Whitlock (1992) for a pure compressible boundary layer.

Fluid	M_1	T_1 (kelvins)	p_1 (atm)	T_w / T_1 Present Study	T_w / T_1 Whitlock(1992)
N_2	2	127.5	1	1.628	1.632
N_2	2	127.5	31.6	1.233	1.24
N_2	2	127.5	36.2	1.16	1.17
SF_6	2	321.9	1	1.139	1.14
SF_6	2	321.9	35.3	1.040	1.039
SF_6	2	321.9	41.0	1.024	1.025

Table 4.4(a) Input and output data for the computation of P_s and P_p : low pressure cases. In each case the shock impingment point corresponds to a local Reynolds number of 2.96 x 10^5.

Fluid	N_2	CO_2	CO_2	AIR
M_1	2	2	2	2
μ_b/μ	0.6	0.0	100	0.6
p_3 / p_1	1.4	1.35	1.35	1.315
p_1 (atm)	1	1	1	0.134
T_1 (kelvins)	127.5	304.1	304.1	308.6
$c_f\|_1$ *1000	1.6	1.52	1.54	1.40
$c_p\|_s$	0.044	0.039	0.04	0.04
$c_p\|_p$	0.067	0.065	0.066	0.068
P_s	1.44	1.42	1.44	1.40
P_p	2.237	2.36	2.38	2.38

Table 4.4(a) Input and output data for the computation of P_s and P_p : low pressure cases, continued. In each case the shock impingment point corresponds to a local Reynolds number of 2.96×10^5.

Fluid	AIR	STEAM	FC-71	SF_6
M_1	2	2	2	2.25
μ_b / μ	0.6	1.0	5	2
p_3 / p_1	1.4	1.352	1.2576	1.32
p_1 (atm)	0.134	8.55	1	1
T_1 (kelvins)	308.6	646.2	646.2	318.7
$c_f\|_1$ *1000	1.55	1.485	1.37	1.45
$c_p\|_s$	0.0393	0.04	0.038	0.0385
$c_p\|_p$	0.0654	0.065	0.064	0.065
P_s	1.313	1.366	1.35	1.435
P_p	2.185	2.219	2.276	2.42

Table 4.4(b) Input and output data for the computation of P_s and P_p : high pressure cases. In each case the shock impingment point corresponds to a local Reynolds number of 2.96 x 10^5.

Fluid	N_2	N_2	SF_6	SF_6
M_1	2	2	2.25	2.25
μ_b / μ	0.6	0.6	2	2
p_3 / p_1	1.4	1.426	1.3	1.215
p_1 (atm)	30.7	36	9	34
T_1 (kelvins)	127.5	127.5	318.7	318.7
$c_f\|_1$ *1000	1.22	0.72	1.45	1.25
$c_p\|_s$	0.036	0.029	0.038	0.033
$c_p\|_p$	0.062	0.041	0.065	0.055
P_s	1.356	1.422	1.4167	1.325
P_p	2.336	2.01	2.448	2.208

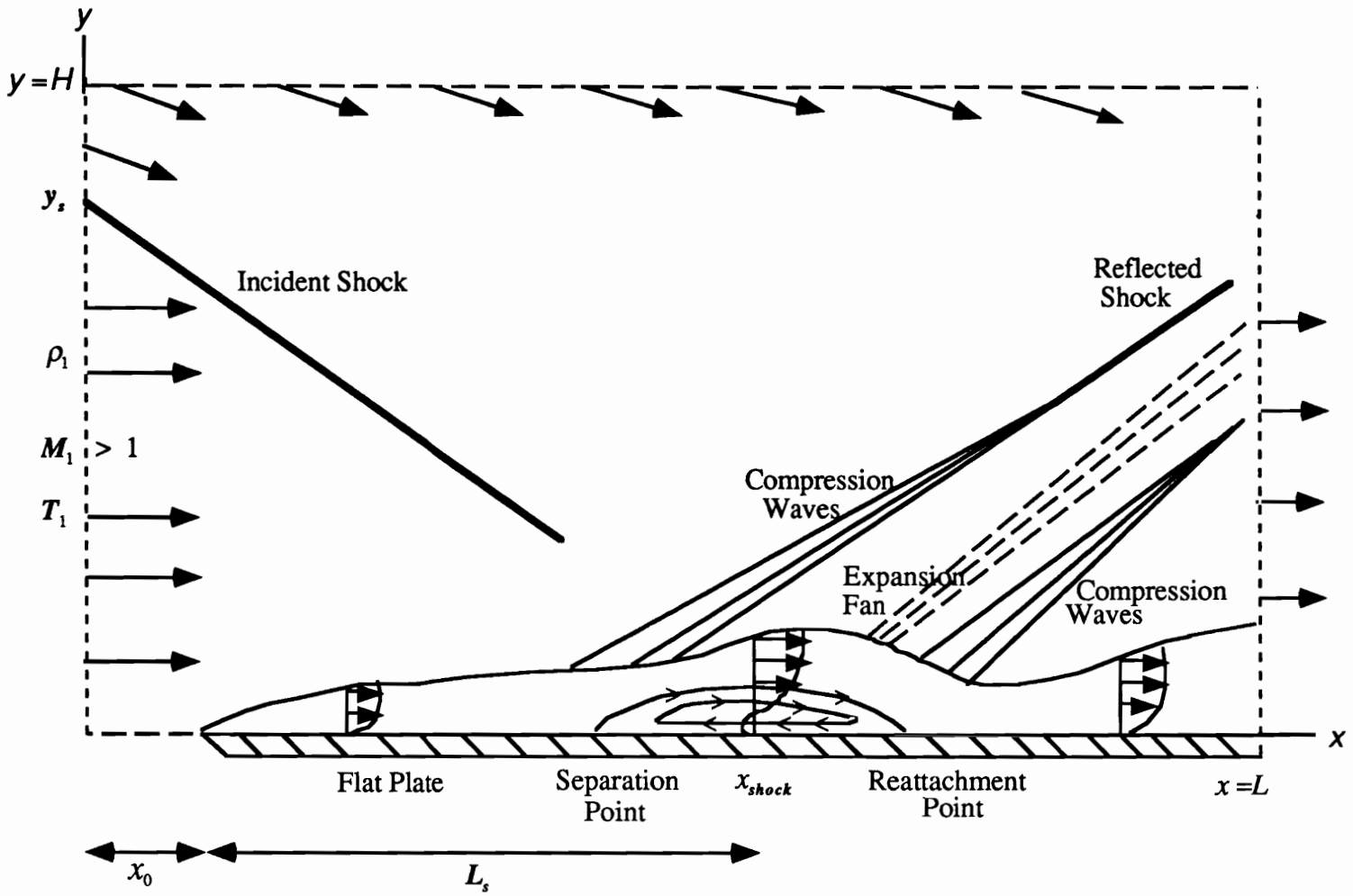

Figure 1.1 Sketch of shock boundary layer interaction.

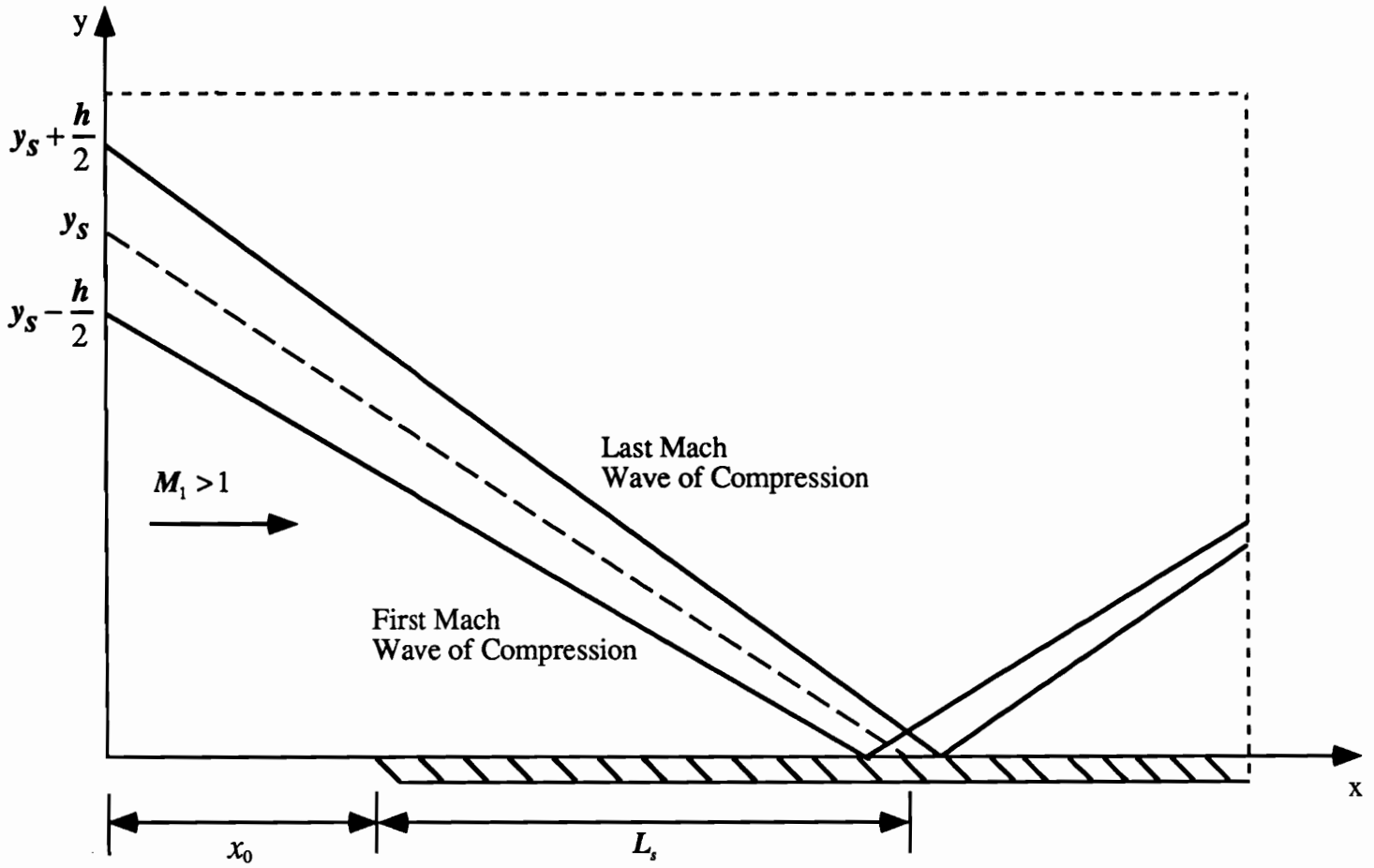

Figure 1.2 Sketch of configuration to illustrate the effect of the width of the incoming signal.

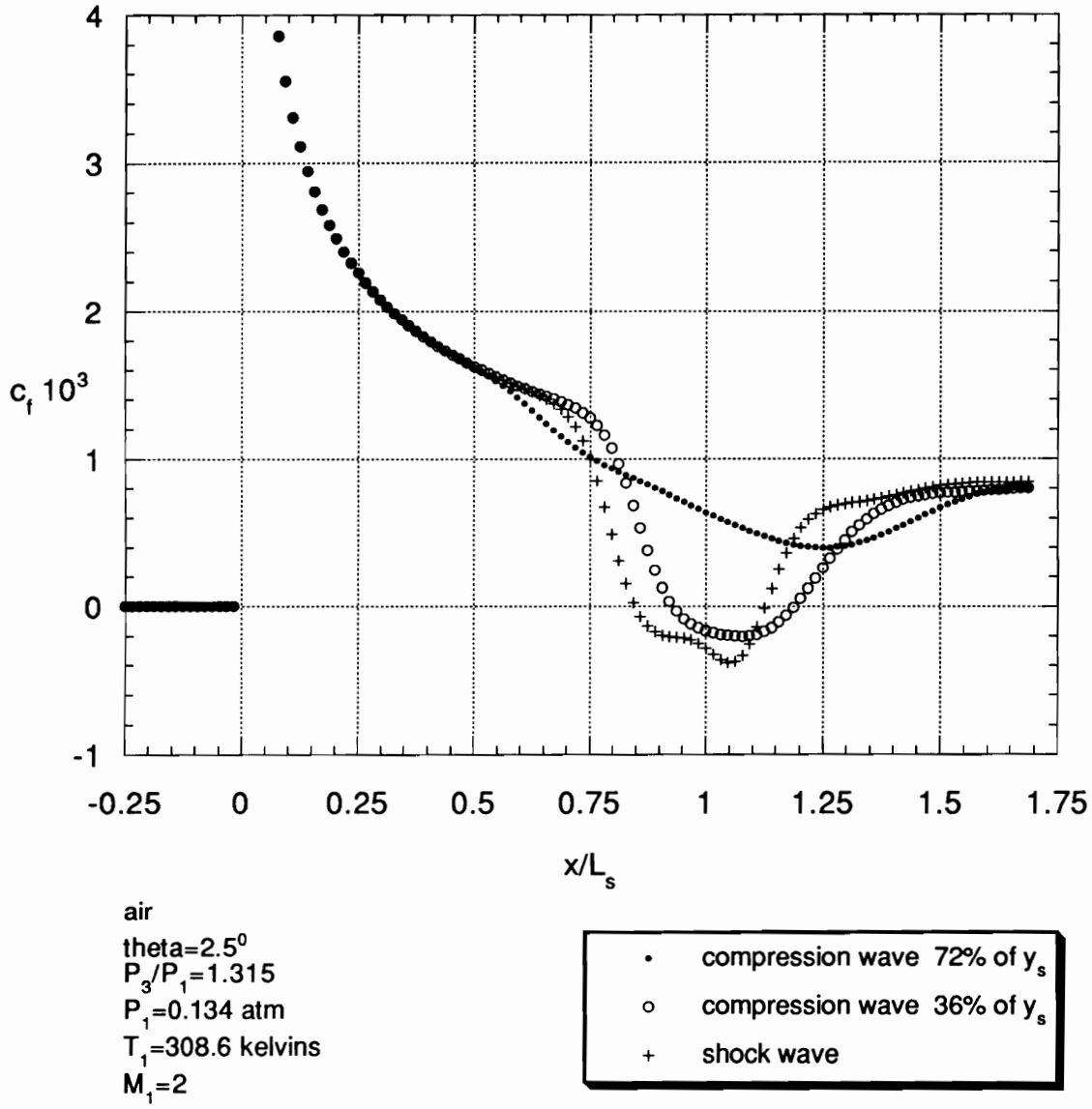

Figure 1.3 Plot of skin friction vs. x/L_s for air with different incoming wave width. The x-axis has been shifted so that the beginning of the plate corresponds to x = 0.

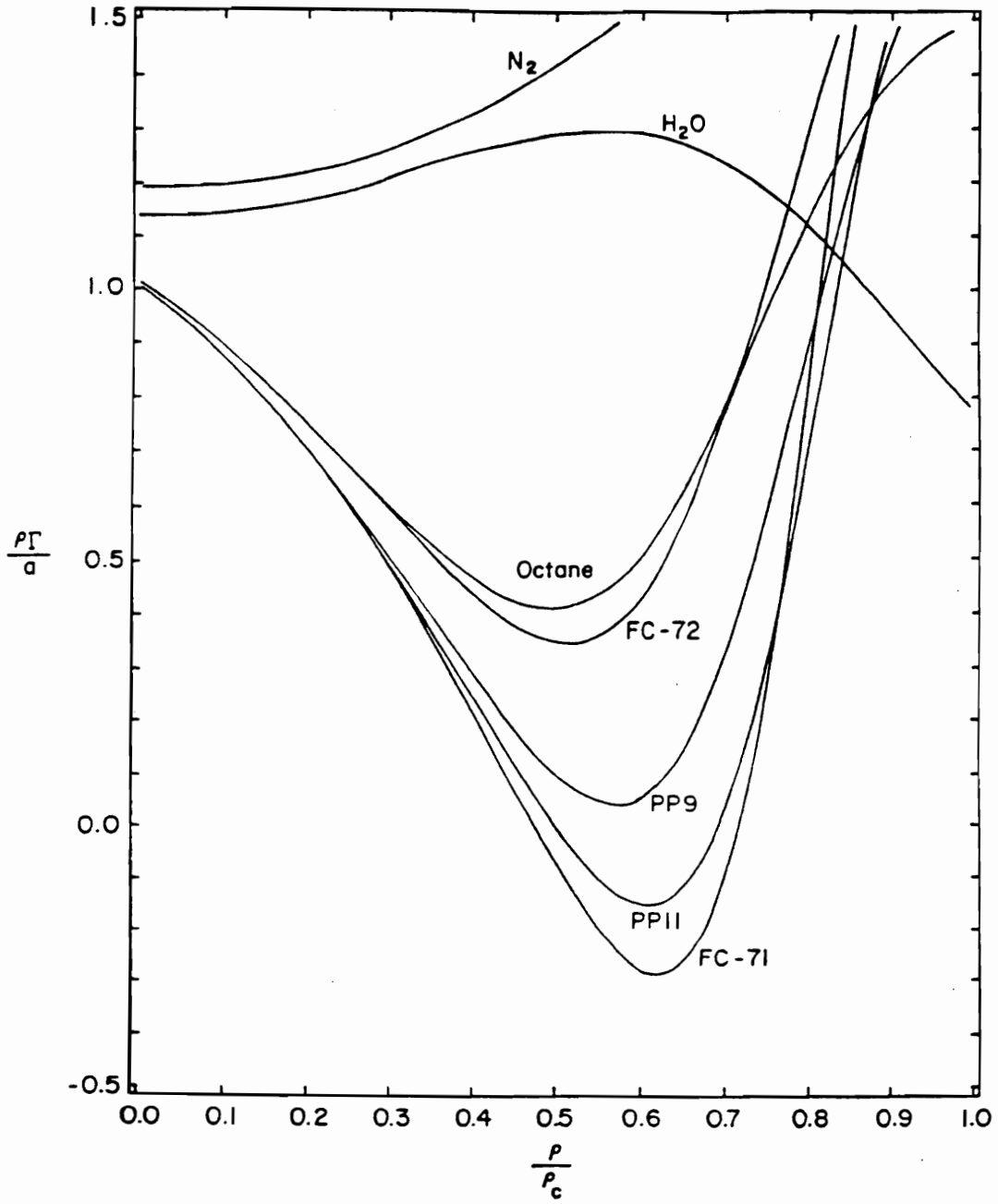

Figure 1.4 Variation of $\rho\Gamma / a$ along the critical isotherm of each fluid. The gas model in each case is that due to Martin Hou (1955) with a power law specific heat.

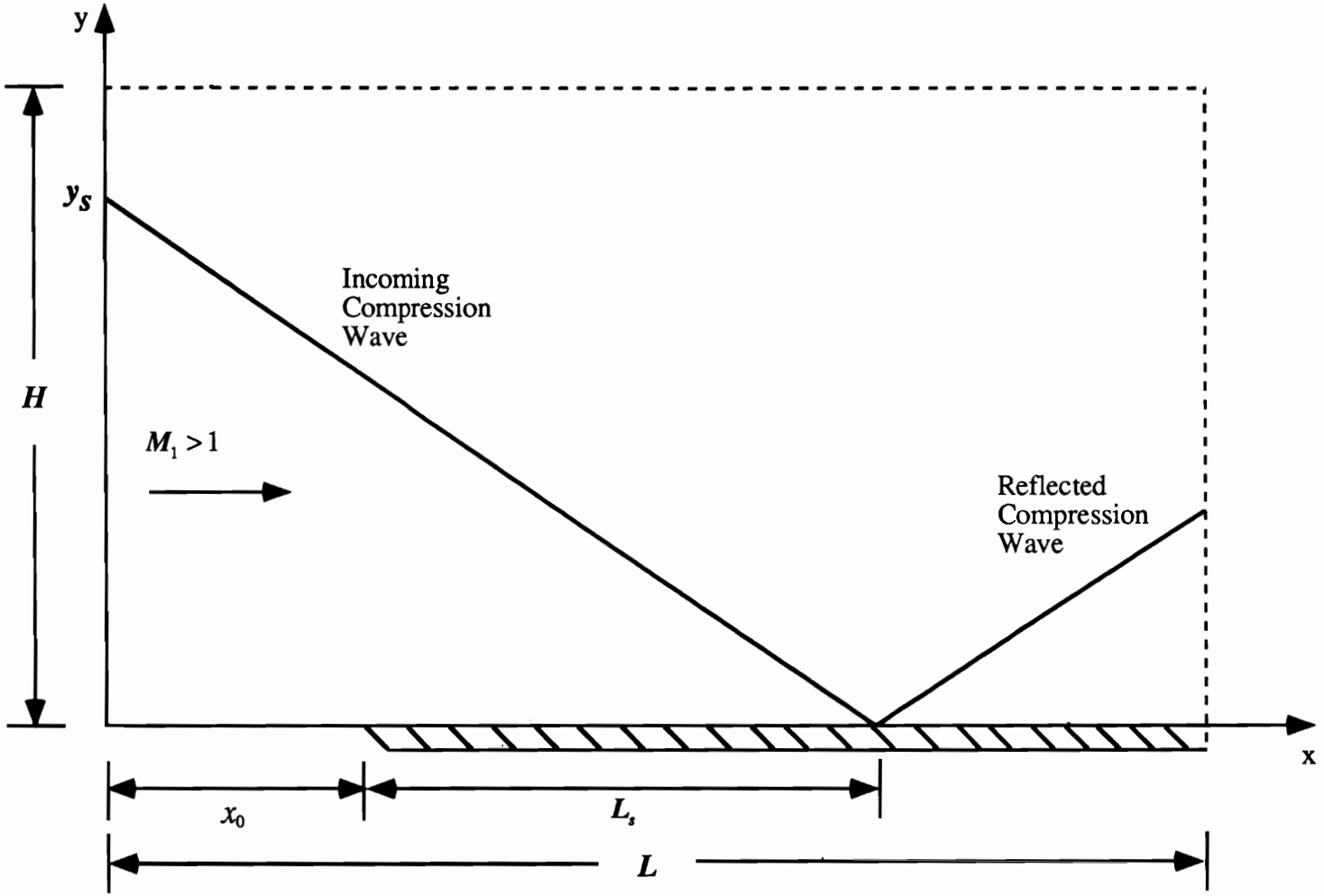

Figure 2.1 Sketch of coordinate system.

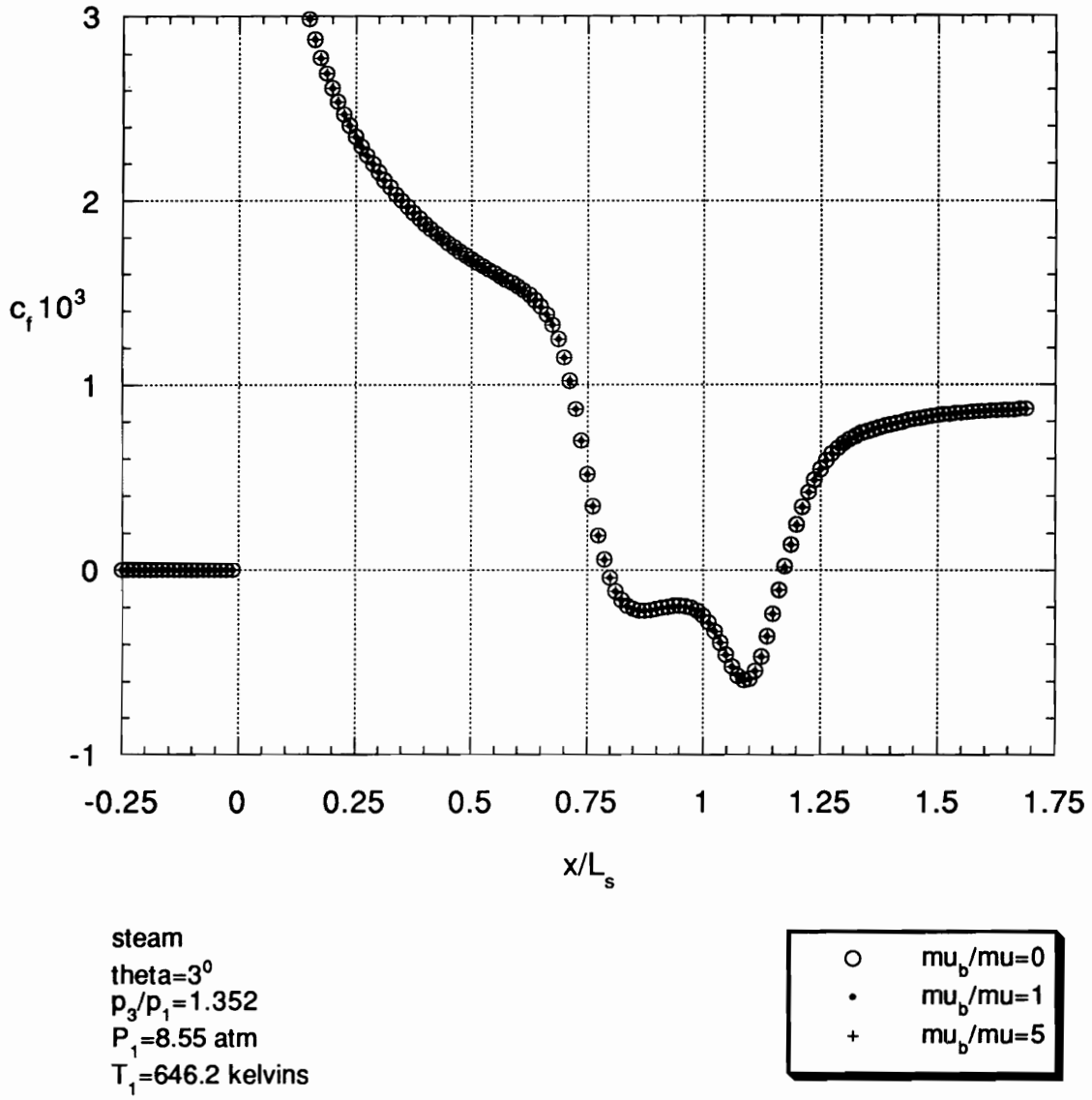

Figure 3.1 Plot of skin friction vs. x/L_s for steam with various bulk viscosities. The x-axis has been shifted so that the beginning of the plate corresponds to x = 0.

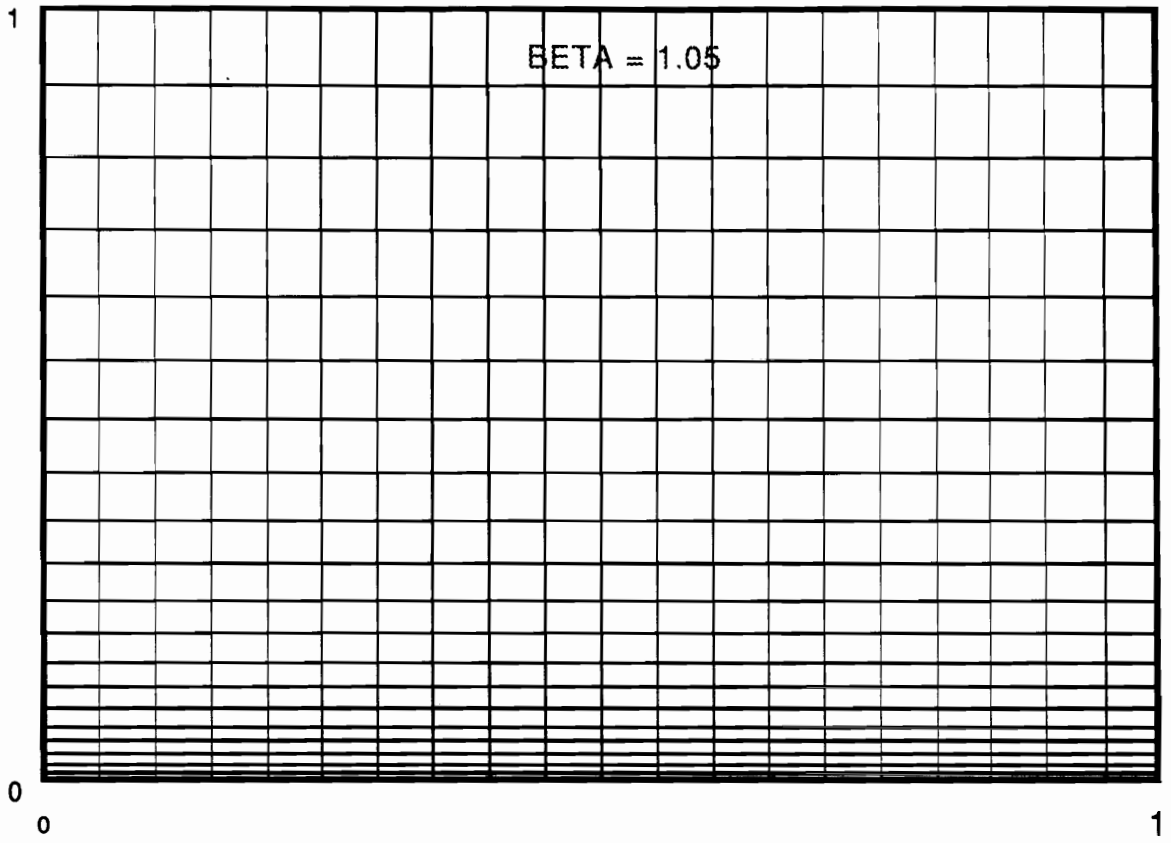

Figure 4.1 Plot of physical domain generated by transformation function (4.1), 21x21 grid.

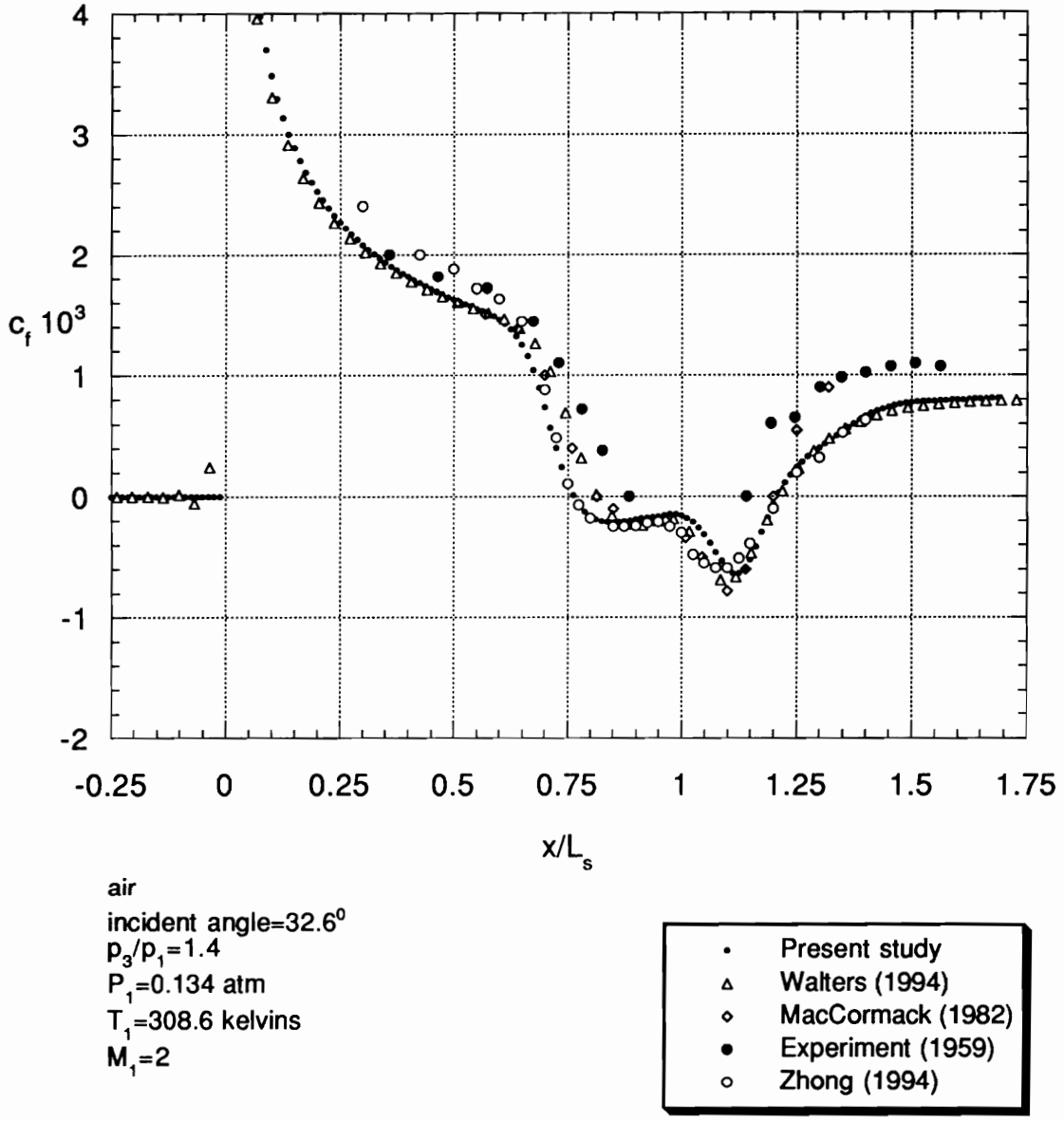

Figure 4.2 Plot of wall skin friction vs. x/L_s for air, ideal-gas case.
The x-axis has been shifted so that the beginning of the plate corresponds to x = 0.

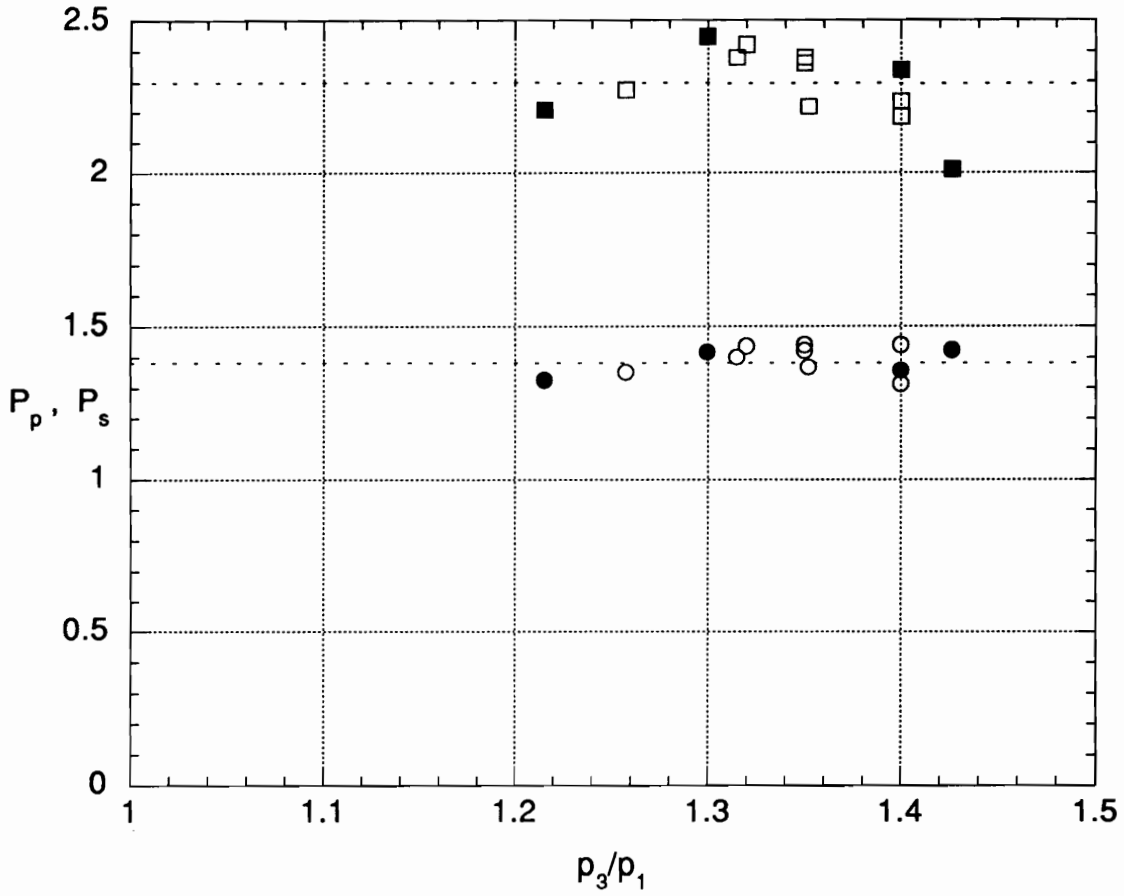

Figure 4.3 P_p or P_s vs. p_3/p_1 for various perfect and dense gases. The data for the perfect gas cases are listed in Table 4.4a and the data for the dense gas cases are given in Table 4.4b.

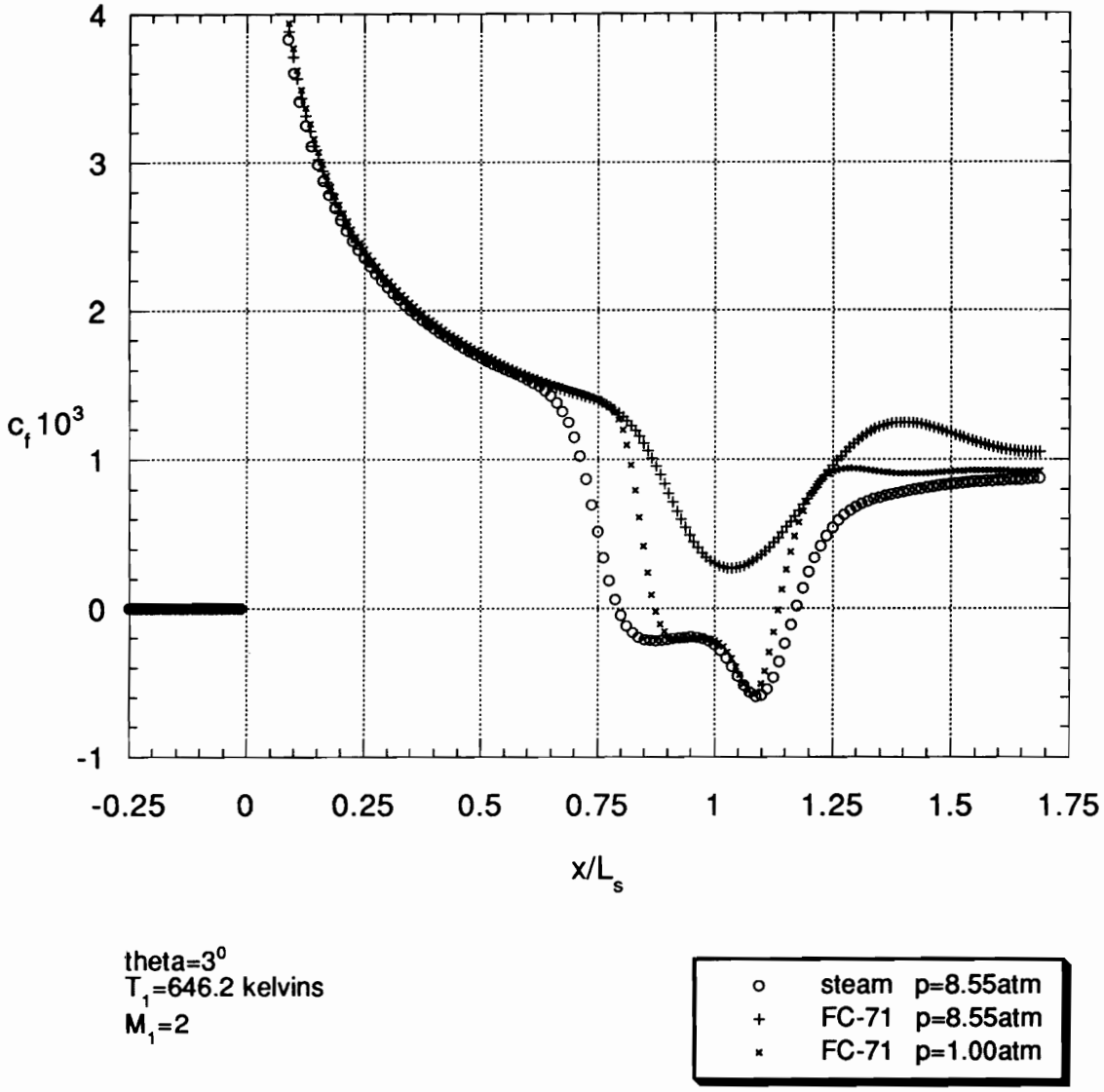

Figure 5.1 Plot of skin friction vs. x/L_s for steam and FC-71.
The x-axis has been shifted so that the beginning of the plate corresponds to x = 0.

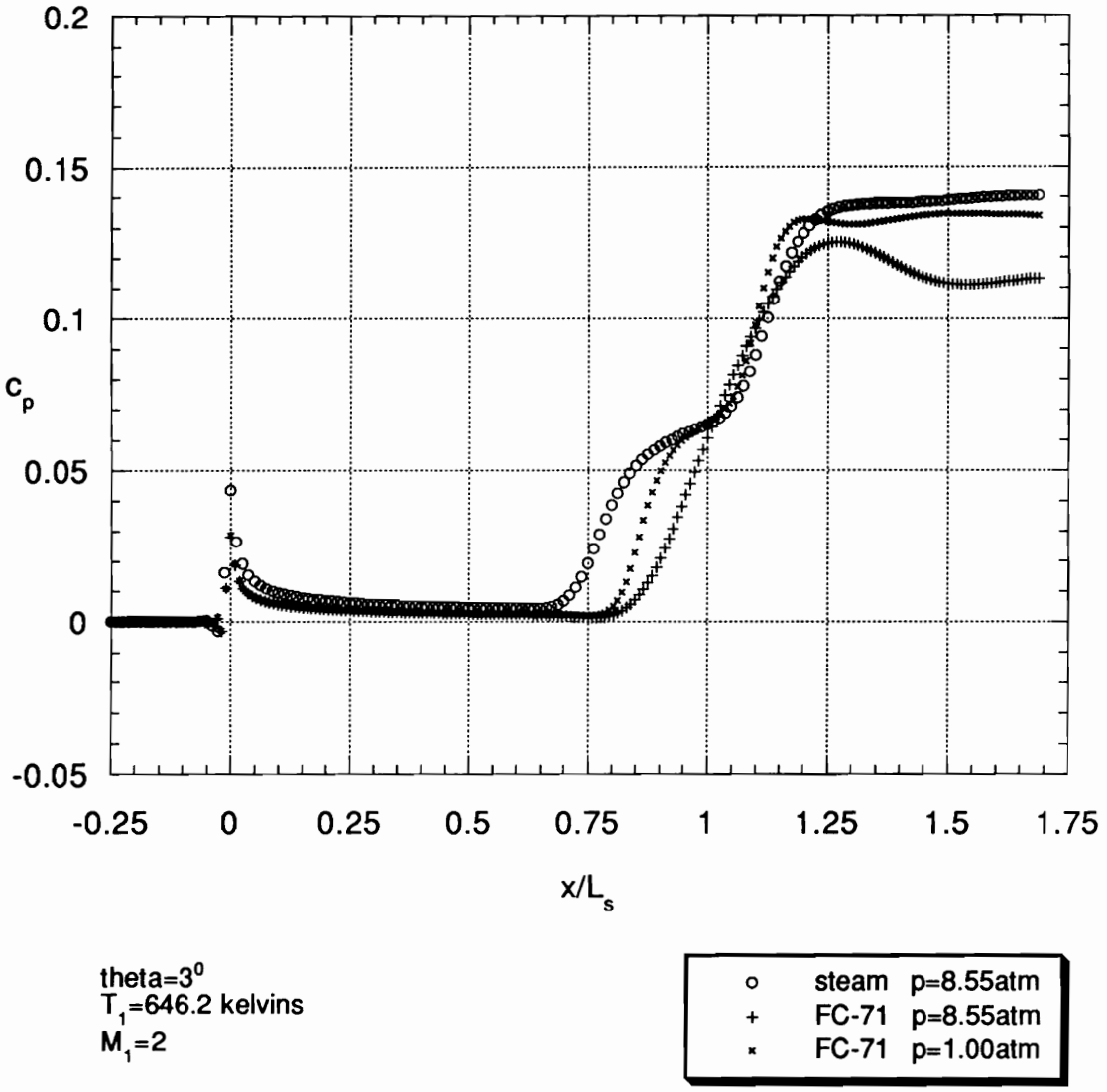

Figure 5.2 Plot of wall pressure coefficient vs. x/L_s for steam and FC-71. The x-axis has been shifted so that the beginning of the plate corresponds to x = 0.

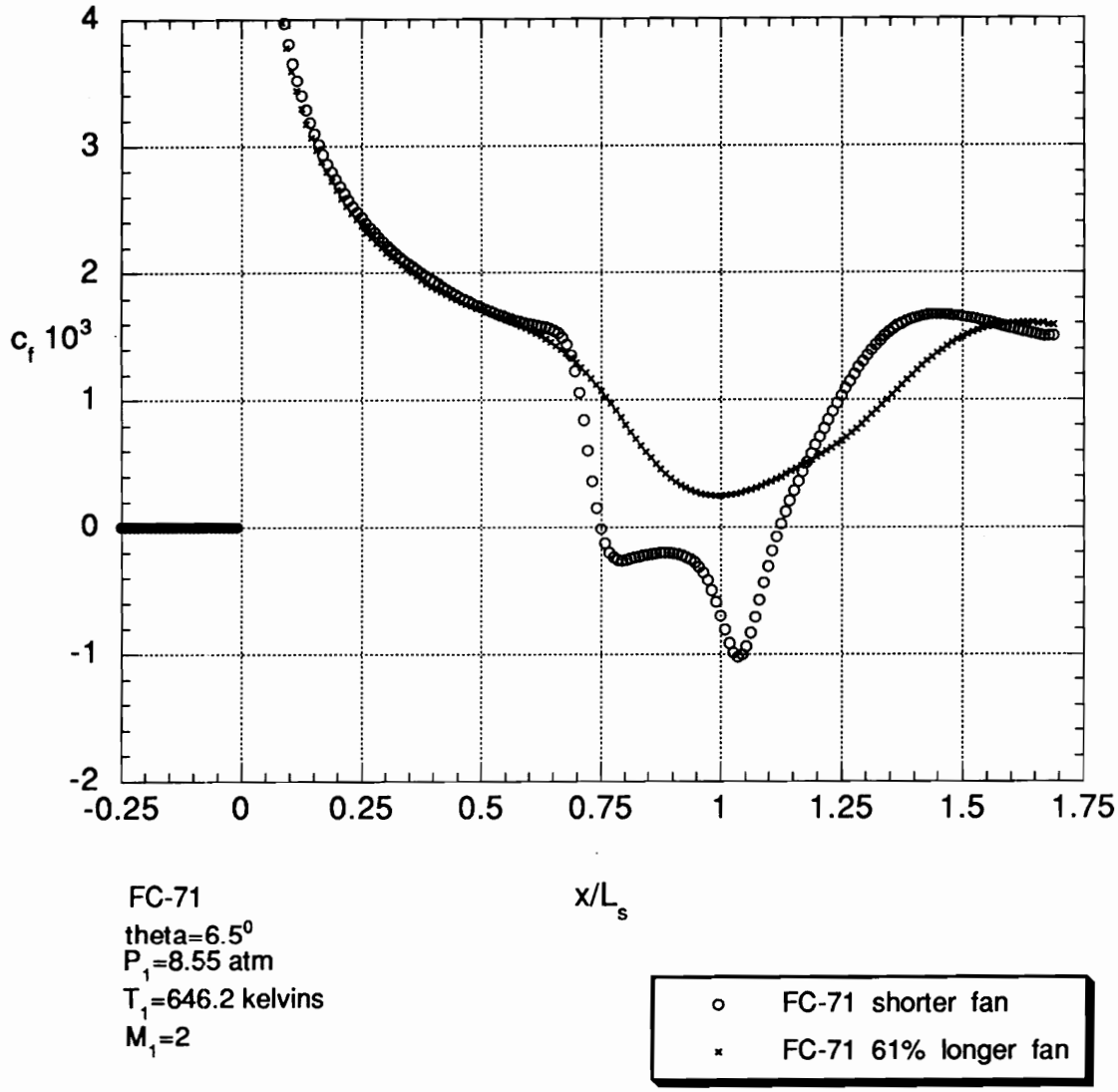

Figure 5.3 Plot of skin friction vs. x/L_s for FC-71 with longer and shorter fans. The x-axis has been shifted so that the beginning of the plate corresponds to x = 0.

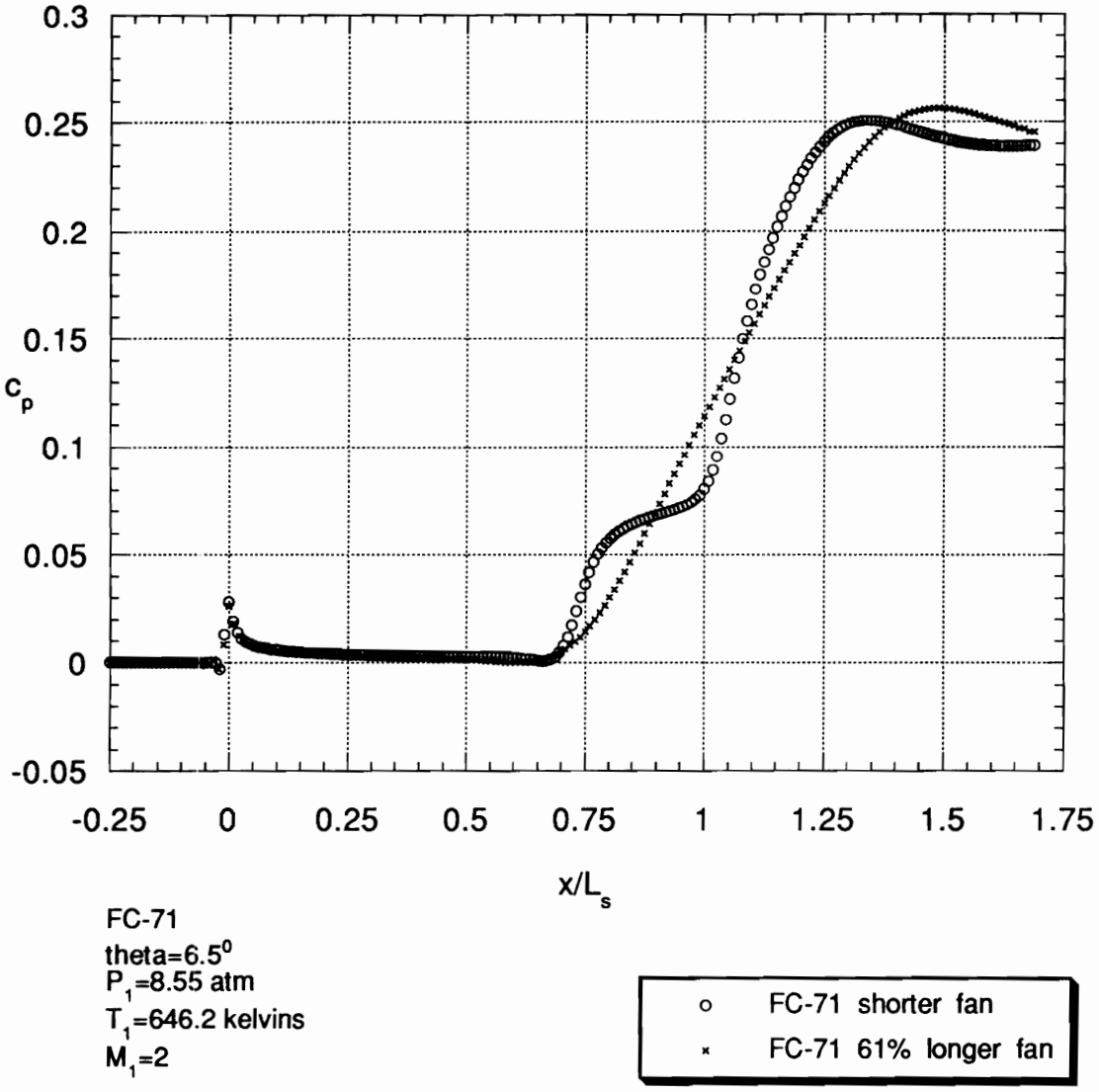

Figure 5.4 Plot of wall pressure coefficient vs. x/L_s for FC-71 with longer and shorter fans.
The x-axis has been shifted so that the beginning of the plate corresponds to x=0.

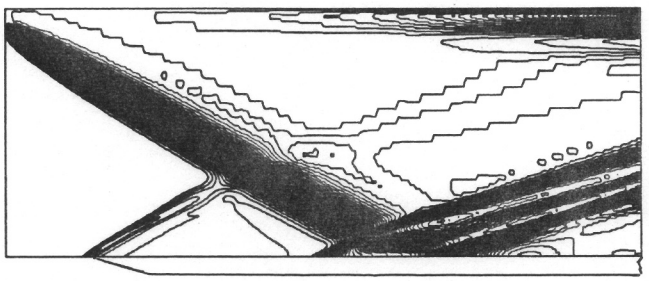

Figure 5.5(a) Contour plot of wall pressure coefficient for FC-71 with shorter fan.

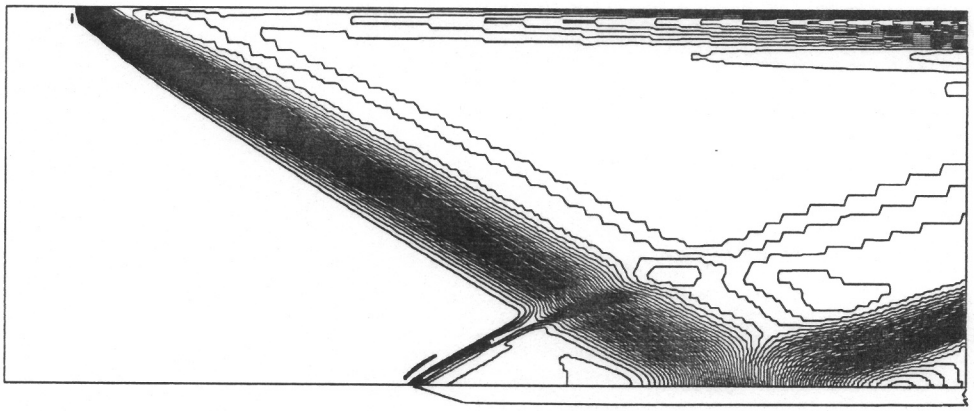

Figure 5.5(b) Contour plot of wall pressure coefficient for FC-71 with longer fan.

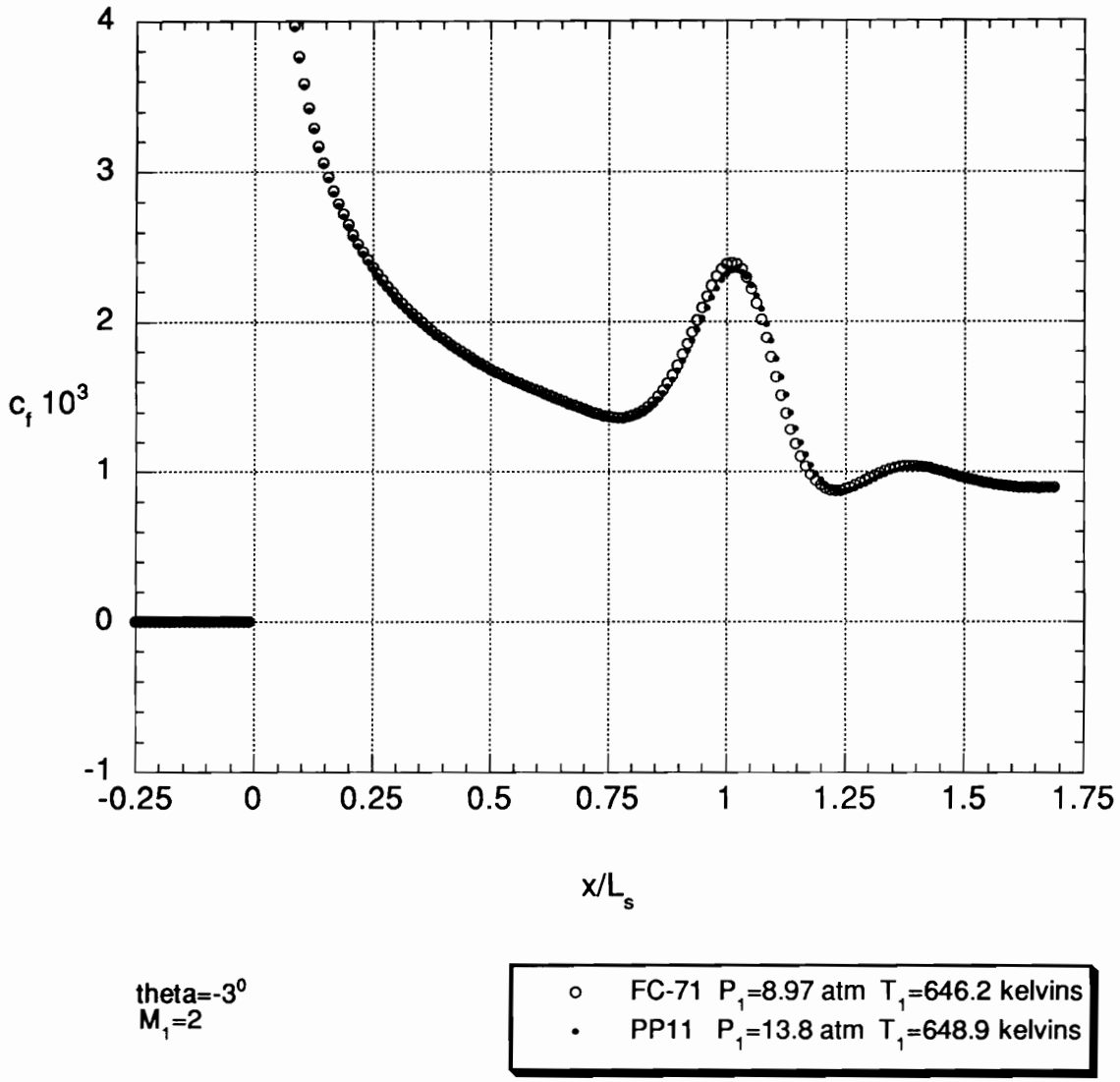

Figure 5.6 Plot of skin friction vs. x/L_s for PP11and FC-71.
The x-axis has been shifted so that the beginning of the plate corresponds to x=0.

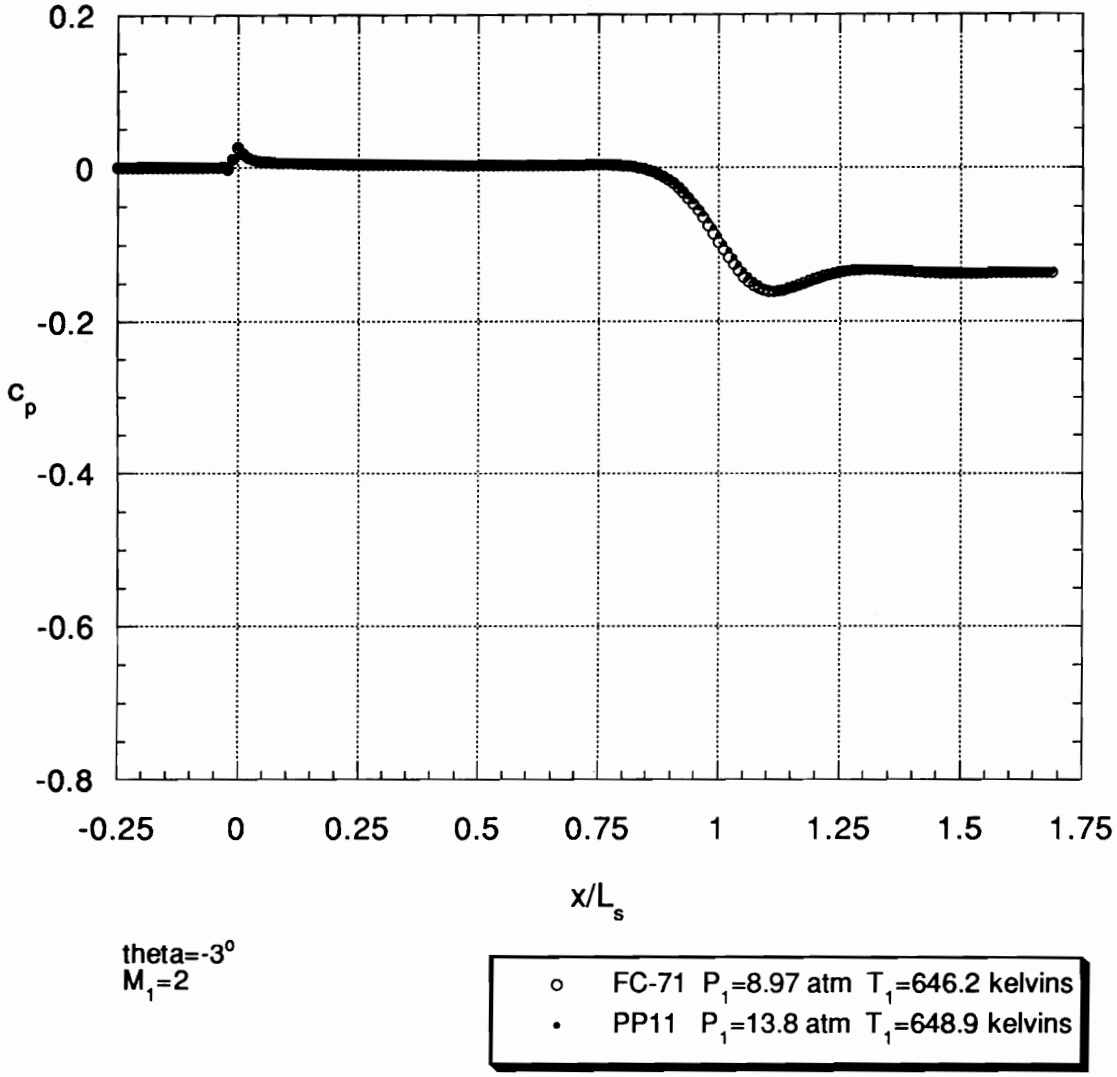

Figure 5.7 Plot of wall pressure coefficient vs. x/L_s for PP11and FC-71. The x-axis has been shifted so that the beginning of the plate corresponds to x=0.

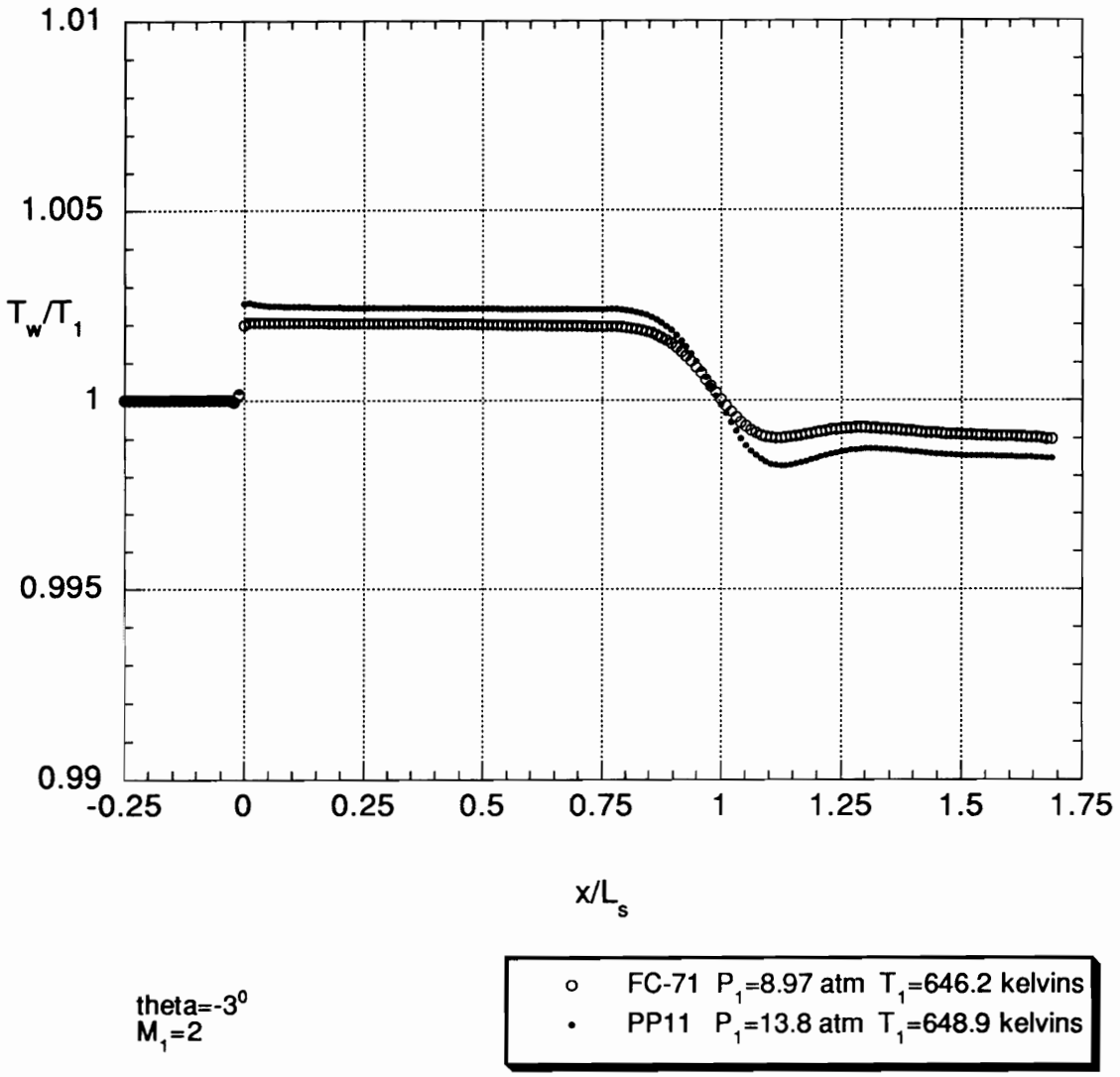

Figure 5.8 Plot of wall temperature vs. x/L_s for PP11and FC-71.
The x-axis has been shifted so that the beginning of the plate corresponds to x=0.

Vita

Sang-Hyuk Park was born on August 4, 1948 in An Sung, Kyunggi-do, Korea. After graduating from An-Sung Elementary School, An-Bob Middle School, and Kyung-Dong High School, he attended Seoul National University which he graduated from in 1977 with his Bachelor of Science degree in Machinery. He served three-year military service from October, 1969 to September, 1972 near DMZ in Korea and returned to the University to continue his study. After Seoul National University he worked for the Hyundai company. He came to USA to do the grauate work in the Mechanical Engineering Department of Colorado State University and received his Master's degree in August, 1981. And then he transferred to Stanford University and received Degree of Engineer in the Mechanical Engineering Department. After Stanford he worked for the Frederiksen Engineering company in Oakland, California.